Probing gravity at cosmic scales

Peirone, S.

COSMOLOGICAL CONSTRAINTS OF A BEYOND-HORNDESKI MODEL

4.1 INTRODUCTION

As mentioned in 1.3.1 it is possible to construct healthy theories beyond Horndeski gravity free from Ostrogradski instabilities. In Gleyzes-Langlois-Piazza-Vernizzi (GLPV) theories [39], for example, there are two extra Lagrangians beyond the Horndeski domain without increasing the extra propagating DOFs [38, 166]. GLPV theories have several peculiar properties: the propagation speeds of matter and the scalar field are mixed [59, 167–169], a partial breaking of the Vainshtein mechanism occurs inside astrophysical bodies [170–175], and a conical singularity can arise at the center of a spherically symmetric and static body [176, 177]. We note that there exist also extensions of Horndeski theories containing higher-order spatial derivatives [178–180] (encompassing Horava gravity [181]) and degenerate higher-order scalar-tensor theories with one scalar propagating DOF [40, 41, 182, 183].

The detection of the gravitational wave (GW) signal GW170817 [61] accompanied by the gamma-ray burst event GRB170817A [184] shows that the speed of GWs c_t is constrained to be in the range $-3 \times 10^{-15} \leq c_t - 1 \leq 7 \times 10^{-16}$ [62] at the redshift $z \leq 0.009$, where we use the unit in which the speed of light c is equivalent to 1. The Horndeski Lagrangian, which gives the exact value $c_t = 1$ without the tuning among functions, is of the form $L = G_4(\phi)R + G_2(\phi, X) + G_3(\phi, X)\Box\phi$, where G_4 is a function of the scalar field ϕ, R is the Ricci scalar, and $G_{2,3}$ depend on both ϕ and $X = \partial^\mu\phi\partial_\mu\phi$ [69–71, 75]. There are also dark energy models in which the GW speed consistent with the above

observational bound of c_t can be realized [185–187]. In GLPV theories with the X dependence in G_4, it is also possible to realize $c_t = 1$ by the existence of an additional quartic Lagrangian beyond the Horndeski domain [188].

In addition to the bound on c_t, the absence of the decay of GWs into dark energy at LIGO/Virgo frequencies ($f \sim 100$ Hz) may imply that the parameter $\alpha_{\rm H}$ characterizing the deviation from Horndeski theories (and whose definition can be found below) is constrained to be very tiny for the scalar sound speed c_s different from 1, typically of order $|\alpha_{\rm H}| \lesssim 10^{-10}$ today [189]. If we literally use this bound, there is little room left for dark energy models in beyondHorndeski theories [190, 191]. If c_s is equivalent to 1, the decay of GWs into dark energy is forbidden. However, it was argued in Ref. [189] that power-law divergent terms would appear, leading to the conclusion that the operator accompanying $\alpha_{\rm H}$ must be suppressed as well [189].

We note that the LIGO/Virgo frequencies are close to those of the typical strong coupling scale or cut-off Λ_c of dark energy models containing derivative field self-interactions [78]. Around this cut-off scale, we cannot exclude the possibility that some ultra-violet (UV) effects come into play to recover the propagation and property of GWs similar to those in General Relativity (GR). If this kind of UV completion occurs around the frequency $f \sim 100$ Hz, the aforementioned bounds on c_t and $\alpha_{\rm H}$ are not applied to the effective field theory of dark energy exploited to describe the cosmological dynamics much below the energy scale Λ_c. Future space-based missions, such as LISA [192], are sensitive to much lower frequencies ($f \sim 10^{-3}$ Hz), so they will offer further valuable information on the properties of GWs with different frequencies.

In GLPV theories, there are constraints on the parameter $\alpha_{\rm H}$ arising from the modifications to gravitational interactions inside astrophysical objects. For example, the consistency of the minimum mass for hydrogen burning in stars with the red dwarf of lowest mass shows

that $|\alpha_{\rm H}|$ is at most of order 0.1 [172, 173, 193, 194]. By using X-ray and lensing profiles of galaxy clusters, similar bounds on $\alpha_{\rm H}$ were obtained in Ref. [174]. From the orbital period of the Hulse-Taylor binary pulsar PSR B1913+1, the upper bound of $|\alpha_{\rm H}|$ is of order 10^{-3} [195]. Cosmological constraints on $\alpha_{\rm H}$ were derived by using particular parametric forms of dimensionless quantities appearing in the effective field theory of dark energy to describe their evolution. In this case, the constraints from CMB and large scale structure data on $|\alpha_{\rm H}|$ are of order $\mathcal{O}(1)$ [196].

In this chapter, we place observational bounds on the beyond Horndeski (BH) dark energy model proposed in Ref. [188] and study how the parameter $\alpha_{\rm H}$ is constrained from the cosmological datasets of CMB temperature anisotropies, baryon acoustic oscillations (BAO), supernovae type Ia (SN Ia), and redshift-space distortions (RSDs). We decide to study also the limit $\alpha_{\rm H} \to 0$ of our theory, which we refer to as Galileon ghost condensate (GGC).

For the likelihood analysis, we will use the publicly available Effective-Field-Theory for `CAMB` (`EFTCAMB`) code[1] [52, 53]. In our investigation the gravitational theory is completely determined by a covariant action, while the analysis in Ref. [196] follows a parameterized approach to GLPV theories. In this respect, the two cosmological models considered are completely different and the constraint on $\alpha_{\rm H}$ obtained in this work cannot be straightforwardly compared to the results in Ref. [196].

The chapter is organized as follows. In Sec 4.2, we briefly review the basics of the BH dark energy model introduced in Ref. [188]. In Sec. 4.3, we show how this model can be implemented in the EFT formulation and derive the background equations of motion together with theoretically consistent conditions. In Sec. 4.4, we discuss the evolution of cosmological perturbations in the presence of matter perfect fluids and investigate the impact of our model on observable quantities. In Sec. 4.5, we present the Monte-Carlo-Markov-Chain (MCMC) constraints on

1 Web page: `http://www.eftcamb.org`

model parameters and compute several information criteria to discuss whether the BH model is favored over the ΛCDM model. Finally, we conclude in Sec. 4.6.

4.2 DARK ENERGY MODEL IN GLPV THEORIES

The dark energy model proposed in Ref. [188] belongs to the quartic-order GLPV theories given by the action

$$\mathcal{S} = \int \mathrm{d}^4x\sqrt{-g}\sum_{i=2}^{4} L_i + \mathcal{S}_M[g_{\mu\nu}, \chi_M]\,, \tag{4.1}$$

where g is the determinant of metric tensor $g_{\mu\nu}$, $\mathcal{S}_M$ is the matter action for all matter fields χ_M, and the Lagrangians $L_{2,3,4}$ are defined by

$$\begin{aligned} L_2 &= G_2(\phi, X)\,, \\ L_3 &= G_3(\phi, X)\Box\phi\,, \\ L_4 &= G_4(\phi, X)R - 2G_{4,X}(\phi, X)\left[(\Box\phi)^2 - \phi^{\mu\nu}\phi_{\mu\nu}\right] \\ &\quad + F_4(\phi, X)\epsilon^{\mu\nu\rho}{}_{\sigma}\epsilon^{\mu'\nu'\rho'\sigma}\phi_{\mu'}\phi_{\mu}\phi_{\nu\nu'}\phi_{\rho\rho'}\,, \end{aligned} \tag{4.2}$$

where $G_{2,3,4}$ and F_4 are functions of the scalar field ϕ and $X = \nabla^\mu\phi\nabla_\mu\phi$, R is the Ricci scalar, and $\epsilon^{\mu\nu\rho\sigma}$ is the totally antisymmetric Levi-Civita tensor satisfying the normalization $\epsilon^{\mu\nu\rho\sigma}\epsilon_{\mu\nu\rho\sigma} = +4!$. We also define $G_{i,X} \equiv \partial G_i/\partial X$ and use the notations $\phi_\mu = \nabla_\mu\phi$ and $\phi_{\mu\nu} = \nabla_\nu\nabla_\mu\phi$ for the covariant derivative operator ∇_μ. We assume that the matter fields χ_M are minimally coupled to gravity.

The last term containing $F_4(\phi, X)$ in L_4 arises beyond the domain of Horndeski theories [39]. The deviation from Horndeski theories can be quantified by the parameter

$$\alpha_{\mathrm{H}} = -\frac{X^2F_4}{G_4 - 2XG_{4,X} + X^2F_4}\,, \tag{4.3}$$

which does not vanish for $F_4 \neq 0$. The line element containing intrinsic tensor perturbations h_{ij} on the flat Friedmann-Lemaître-Robertson-Walker (FLRW) space-time is given by

$$ds^2 = -dt^2 + a^2(t)\left(\delta_{ij} + h_{ij}\right) dx^i dx^j , \tag{4.4}$$

where $a(t)$ is the time-dependent scale factor, and h_{ij} satisfies the transverse and traceless conditions ($\nabla^j h_{ij} = 0$ and $h_i{}^i = 0$). The propagation speed squared of tensor perturbations is [39, 167, 168]

$$c_t^2 = \frac{G_4}{G_4 - 2XG_{4,X} + X^2 F_4} . \tag{4.5}$$

In quartic-order Horndeski theories ($F_4 = 0$), the X dependence in G_4 leads to the difference of c_t^2 from 1. In GLPV theories, it is possible to realize $c_t^2 = 1$ for the function

$$F_4 = \frac{2G_{4,X}}{X} , \tag{4.6}$$

under which $\alpha_{\rm H} = -2XG_{4,X}/G_4$.

Here we will study observational constraints on the model proposed in Ref. [188]. This is characterized by the following functions

$$\begin{aligned} G_2 &= a_1 X + a_2 X^2 , \qquad G_3 = 3a_3 X , \\ G_4 &= \frac{m_0^2}{2} - a_4 X^2 , \qquad F_4 = -4a_4 , \end{aligned} \tag{4.7}$$

where m_0 and $a_{1,2,3,4}$ are constants. This beyondHorndeski model, hereafter BH, satisfies the condition (4.6), and hence $c_t^2 = 1$. When $a_4 = 0$, all the departures from Horndeski are suppressed. We refer to this limit of BH as Galileon Ghost Condensate (GGC) model. Taking the limits $a_2 \to 0$ and $a_3 \to 0$, GGC recovers the cubic covariant Galileon [28, 141] and ghost condensate [197], respectively.

The BH model allows for the existence of self-accelerating de Sitter solutions finally approaching constant values of X. Before approaching

the de Sitter attractor, the dark energy equation of state $w_{\rm DE}$ can exhibit a phantom behavior (i.e., $w_{\rm DE} < -1$) without the appearance of ghosts [188]. The cubic covariant Galileon gives rise to the tracker solution with $w_{\rm DE} = -2$ in the matter era [29], but this evolution is incompatible with the joint data analysis of CMB, BAO, and SN Ia [30]. On the other hand, in both BH and GGC, the $a_2 X^2$ term works to prevent for approaching the tracker, so that $-2 < w_{\rm DE} < -1$ in the matter era.

The BH model leads to the evolution of cosmological perturbations different from that in GR. The late-time modification to the cosmic growth rate arises mostly from the cubic Galileon term $3a_3 X\Box\phi$ [188, 198].

4.3 METHODOLOGY

In this section, we discuss the evolution of the background and linear scalar perturbations in the BH model. We make use of the `EFTCAMB/EFTCosmoMC` codes [52, 53], in which the EFT of dark energy and modified gravity [42–45, 48] is implemented into `CAMB/CosmoMC` [51, 58]. The EFT framework enables one to deal with any dark energy and modified gravity model with one scalar propagating DOF ϕ in a unified and model-independent manner.

The EFT of dark energy is based on the 3+1 Arnowitt-Deser-Misner (ADM) decomposition of spacetime [199] given by the line element

$$ds^2 = -N^2\,dt^2 + h_{ij}\left(dx^i + N^i\,dt\right)\left(dx^j + N^j\,dt\right), \tag{4.8}$$

where N is the lapse, N^i is the shift vector, and h_{ij} is the three-dimensional metric. A unit vector orthogonal to the constant time hyper-surface Σ_t is given by $n_\mu = N\nabla_\mu t = (N, 0, 0, 0)$. The extrinsic curvature is defined by $K_{ij} = h_i^k \nabla_k n_j$. The internal geometry of Σ_t is quantified by the three-dimensional Ricci tensor $\mathcal{R}_{ij} = {}^{(3)}R_{ij}$ associated with the metric h_{ij}.

On the flat FLRW background, we consider the line element containing three scalar metric perturbations δN, ψ, and ζ, as

$$\begin{aligned} \mathrm{d}s^2 = &-(1+2\delta N)\,\mathrm{d}t^2 + 2\partial_i\psi\,\mathrm{d}t\,\mathrm{d}x^i \\ &+ a^2(t)(1+2\zeta)\delta_{ij}\,\mathrm{d}x^i\,\mathrm{d}x^j\,, \end{aligned} \tag{4.9}$$

where $\partial_i \equiv \partial/\partial x^i$. We also choose the the unitary gauge in which the perturbation $\delta\phi$ of the scalar field ϕ vanishes. Then, the perturbations of extrinsic and intrinsic curvatures are expressed as [44, 48, 167, 179]

$$\delta K_{ij} = a^2\left(H\delta N - 2H\zeta - \dot{\zeta}\right)\delta_{ij} + \partial_i\partial_j\psi\,, \tag{4.10}$$

$$\delta\mathcal{R}_{ij} = -\delta_{ij}\partial^2\zeta - \partial_i\partial_j\zeta\,, \tag{4.11}$$

where $\partial^2 \equiv \delta^{kl}\partial_k\partial_l$, and $H = \dot{a}/a$ is the Hubble expansion rate, and a dot represents a derivative with respect to t. The perturbations of traces $K \equiv K^i{}_i$ and $\mathcal{R} \equiv \mathcal{R}^i{}_i$ are denoted as δK and $\delta\mathcal{R}$, respectively, with $\delta g^{00} = 2\delta N$.

In the ADM language, the Lagrangian of GLPV theories depends on the scalar quantities N, K, $K_{ij}K^{ij}$, $\mathcal{R}$, $K_{ij}\mathcal{R}^{ij}$, and t [44]. Expanding the corresponding action up to second order in scalar perturbations of those quantities, it follows that

$$\begin{aligned} \mathcal{S} = \int \mathrm{d}^4x\sqrt{-g}\,m_0^2\Bigg\{ &\frac{1}{2}\left[1+\Omega(a)\right]R + \frac{\Lambda(a)}{m_0^2} - \frac{c(a)}{m_0^2}\delta g^{00} \\ &+ H_0^2\frac{\gamma_1(a)}{2}\left(\delta g^{00}\right)^2 - H_0\frac{\gamma_2(a)}{2}\,\delta g^{00}\,\delta K \\ &- H_0^2\frac{\gamma_3(a)}{2}\left(\delta K\right)^2 - H_0^2\frac{\gamma_4(a)}{2}\,\delta K^i_j\delta K^j_i \\ &+ \frac{\gamma_5(a)}{2}\delta g^{00}\delta\mathcal{R}\Bigg\} + \mathcal{S}_M[g_{\mu\nu},\chi_M]\,, \end{aligned} \tag{4.12}$$

where m_0 is a constant having a dimension of mass, and Ω, Λ, c, γ_i are called EFT functions that depend on the background scale factor a. The explicit relations between those EFT functions and the functions $G_{2,3,4}$, F_4 in the action (4.1) are given in Ref. [200].

The first three variables Ω, Λ, c determine both the background evolution and linear perturbations, whereas the functions γ_i solely appear at the level of linear perturbations. For the matter action $\mathcal{S}_M$, we take dark matter and baryons (background density ρ_m and vanishing pressure) and radiation (background density ρ_r and pressure $P_r = \rho_r/3$) into account. Then, the background equations are expressed as [42, 43]

$$3m_0^2H^2 = \rho_{\rm DE} + \rho_m + \rho_r\,, \tag{4.13}$$
$$-m_0^2\left(2\dot{H} + 3H^2\right) = P_{\rm DE} + P_r\,, \tag{4.14}$$

where

$$\rho_{\rm DE} = 2c - \Lambda - 3m_0^2H\left(\dot{\Omega} + H\Omega\right)\,, \tag{4.15}$$
$$P_{\rm DE} = \Lambda + m_0^2\left[\ddot{\Omega} + 2H\dot{\Omega} + \Omega\left(2\dot{H} + 3H^2\right)\right]. \tag{4.16}$$

The density $\rho_{\rm DE}$ and pressure $P_{\rm DE}$ of dark energy obey the continuity equation

$$\dot{\rho}_{\rm DE} + 3H\left(\rho_{\rm DE} + P_{\rm DE}\right) = 0\,. \tag{4.17}$$

In GLPV theories, there is the specific relation $\gamma_3 = -\gamma_4$. If we restrict the theories to those satisfying $c_t^2 = 1$, it follows that $\gamma_4 = 0$. Then, the model given by the functions (4.7) corresponds to the coefficients

$$\gamma_3 = 0\,, \qquad \gamma_4 = 0\,, \tag{4.18}$$

so that we are left with three functions $\gamma_1, \gamma_2, \gamma_5$ at the level of linear perturbations.

To study the cosmological evolution of our model in `EFTCAMB`, we first solve the background equations of motion and then map to the EFT functions according to the procedure given in Refs. [42–45, 48, 180, 200].

4.3.1 *Background equations in the BH model*

For the model (4.7), the background equations are given by Eqs. (4.13) and (4.14), with

$$\Omega = -\frac{2a_4\dot{\phi}^4}{m_0^2}\,, \tag{4.19}$$

and

$$\rho_{\rm DE} = -a_1\dot{\phi}^2 + 3a_2\dot{\phi}^4 + 18a_3H\dot{\phi}^3 + 30a_4H^2\dot{\phi}^4\,, \tag{4.20}$$

$$P_{\rm DE} = -a_1\dot{\phi}^2 + a_2\dot{\phi}^4 - 6a_3\dot{\phi}^2\ddot{\phi} - 2a_4\dot{\phi}^3\left[8H\ddot{\phi} + \dot{\phi}(2\dot{H} + 3H^2)\right]\,. \tag{4.21}$$

The parameters c and Λ in Eqs. (4.15) and (4.16) can be expressed in terms of quantities on the right hand sides of Eqs. (4.20) and (4.21). Following Ref. [188], we define the dimensionless variables (density parameters):

$$x_1 = -\frac{a_1\dot{\phi}^2}{3m_0^2H^2}\,, \qquad x_2 = \frac{a_2\dot{\phi}^4}{m_0^2H^2}\,,$$
$$x_3 = \frac{6a_3\dot{\phi}^3}{m_0^2H}\,, \qquad x_4 = \frac{10a_4\dot{\phi}^4}{m_0^2}\,, \tag{4.22}$$

and

$$\Omega_{\rm DE} = \frac{\rho_{\rm DE}}{3m_0^2H^2}\,, \quad \Omega_m = \frac{\rho_m}{3m_0^2H^2}\,, \quad \Omega_r = \frac{\rho_r}{3m_0^2H^2}\,. \tag{4.23}$$

From Eq. (4.13), we have

$$\Omega_m = 1 - \Omega_{\rm DE} - \Omega_r\,, \tag{4.24}$$

where the dark energy density parameter is given by

$$\Omega_{\rm DE} = x_1 + x_2 + x_3 + x_4\,. \tag{4.25}$$

In terms of x_4, the deviation parameter (4.3) from Horndeski theories is expressed as

$$\alpha_{\rm H} = \frac{4x_4}{5-x_4}\,, \tag{4.26}$$

and hence $\alpha_{\rm H}$ is of the same order as x_4 for $|x_4| \leq 1$.

The variables $x_{1,2,3,4}$ and Ω_r are known by solving the ordinary differential equations

$$x_1' = 2x_1(\epsilon_\phi - h)\,, \tag{4.27}$$
$$x_2' = 2x_2(2\epsilon_\phi - h)\,, \tag{4.28}$$
$$x_3' = x_3(3\epsilon_\phi - h)\,, \tag{4.29}$$
$$x_4' = 4x_4\epsilon_\phi\,, \tag{4.30}$$
$$\Omega_r' = -2\Omega_r(2+h)\,, \tag{4.31}$$

where a prime denotes the derivative with respect to $\mathcal{N} = \ln(a)$. On using Eqs. (4.13) and (4.14), it follows that

$$\begin{aligned}
\epsilon_\phi &\equiv \frac{\ddot{\phi}}{H\dot{\phi}} \\
&= -\frac{1}{q_s}\Big[20(3x_1+2x_2) - 5x_3(3x_1+x_2+\Omega_r-3) \\
&\quad - x_4(36x_1+16x_2+3x_3+8\Omega_r)\Big]\,, \\
h &\equiv \frac{\dot{H}}{H^2} \\
&= -\frac{1}{q_s}[10(3x_1+x_2+\Omega_r+3)(x_1+2x_2) \\
&\quad + 10x_3(6x_1+3x_2+\Omega_r+3) + 15x_3^2 \\
&\quad + x_4(78x_1+32x_2+30x_3+12\Omega_r+36) + 12x_4^2]\,,
\end{aligned}$$

with

$$q_s \equiv 20(x_1 + 2x_2 + x_3) + 4x_4(6 - x_1 - 2x_2 + 3x_3) + 5x_3^2 + 8x_4^2 . \quad (4.32)$$

For a given set of initial conditions $x_{1,2,3,4}$ and Ω_r, we can solve Eqs. (4.27)-(4.31) to determine the evolution of density parameters as well as ϕ and H. Practically, we start to solve the above dynamical system at redshift $z_s = 1.5 \times 10^5$ and iteratively scan over initial conditions leading to the viable cosmology satisfying the constraint (4.24) today ($z = 0$). Additionally, evaluating Eq. (4.25) at present time, we can eliminate one model parameter, for example $x_2^{(0)}$, as $x_2^{(0)} = \Omega_{\rm DE}^{(0)} - x_1^{(0)} - x_3^{(0)} - x_4^{(0)}$, where "(0)" represents today's quantities.

4.3.2 *Mapping*

To study the evolution of scalar perturbations and observational constraints on dark energy models in `EFTCAMB`, it is convenient to use the mapping between EFT functions and model parameters in BH. In Sec. 4.3.1, we already discussed the mapping of the background quantities Ω, Λ and c. The functions $\gamma_{1,2,5}$, which are associated with scalar perturbations, are given by

$$\gamma_1 = \frac{H^2}{H_0^2}\left[\frac{1}{20}\left(24x_4 - hx_4' + 3x_4' - x_4''\right) + 2x_2 + \frac{1}{12}\left\{(h+9)\,x_3 + x_3'\right\}\right], \quad (4.33)$$

$$\gamma_2 = \frac{H}{H_0}\left[\frac{1}{5}\left(x_4' - 8x_4\right) - x_3\right], \quad (4.34)$$

$$\gamma_5 = \frac{2}{5}x_4. \quad (4.35)$$

The expressions of these EFT functions allow us to draw already some insight about the contributions of each x_i to the dynamics of linear perturbations. In general, the variable γ_1 cannot be well constrained by data being its contribution to the observables below the cosmic variance [201]. The main modification to the evolution of perturbations compared to GR arises from γ_2 and γ_5, which are mostly affected by x_3 and x_4. The variables x_1 and x_2 contribute to the perturbation dynamics through the Hubble expansion rate H in γ_2.

4.3.3 *Viability constraints*

There are theoretically consistent conditions under which the perturbations are not plagued by the appearance of ghosts and Laplacian instabilities in the small-scale limit. For the BH model (4.7), the conditions for the absence of ghosts in tensor and scalar sectors are given, respectively, by [188]

$$Q_t = \frac{5 - x_4}{10} m_0^2 > 0\,, \tag{4.36}$$

$$Q_s = \frac{3(5 - x_4) q_s}{25(x_3 + 2x_4 - 2)^2} m_0^2 > 0\,, \tag{4.37}$$

where q_s is defined in Eq. (4.32). Then, we have the following constraints

$$x_4 < 5\,, \qquad q_s > 0\,. \tag{4.38}$$

The BH model has the property $c_t^2 = 1$, so there is no Laplacian instability for tensor perturbations. We note that the reduced Planck mass $M_{\rm pl}$ is related to m_0 according to the relation $M_{\rm pl}^2 = m_0^2(1 + \Omega_0)$ in the local environment with screened fifth forces [170], where Ω_0

is today's value of Ω. Then, the Newton gravitational constant $G_{\rm N}$ is given by

$$G_{\rm N} = \frac{1}{8\pi M_{\rm pl}^2} = \frac{1}{8\pi m_0^2}\left(1 - \frac{x_4^{(0)}}{5}\right)^{-1}, \tag{4.39}$$

which is positive under the absence of tensor ghosts.

For scalar perturbations, there are three propagation speed squares c_s^2, $\tilde{c}_r^2$, and $\tilde{c}_m^2$ associated with the scalar field ϕ, radiation, and nonrelativistic matter, respectively. In Horndeski theories, they are not coupled to each other, so that the propagation speed squares of radiation and nonrelativistic matter are given, respectively, by $c_r^2 = 1/3$ and $c_m^2 = +0$. In GLPV theories, they are generally mixed with each other, apart from $\tilde{c}_m^2$ (which has the value $\tilde{c}_m^2 = +0$) [39, 59, 167–169]. Then, the Laplacian instabilities of scalar perturbations can be avoided under the two conditions

$$c_s^2 = \frac{1}{2}\left(c_r^2 + c_{\rm H}^2 - \beta_{\rm H} - \gamma_{\rm H}\right) > 0\,, \tag{4.40}$$

$$\tilde{c}_r^2 = \frac{1}{2}\left(c_r^2 + c_{\rm H}^2 - \beta_{\rm H} + \gamma_{\rm H}\right) > 0\,, \tag{4.41}$$

where

$$\begin{aligned}
c_{\rm H}^2 &= \frac{2}{Q_s}\left[\dot{\mathcal{M}} + H\mathcal{M} - Q_t - \frac{3\rho_m + 4\rho_r}{12H^2(1+\alpha_{\rm B})^2}\right],\\
\beta_r &= \frac{4\alpha_{\rm H}\rho_r}{3Q_sH^2(1+\alpha_{\rm B})^2}\,, \quad \beta_m = \frac{\alpha_{\rm H}\rho_m}{Q_sH^2(1+\alpha_{\rm B})^2}\,,\\
\mathcal{M} &= \frac{Q_t(1+\alpha_{\rm H})}{H(1+\alpha_{\rm B})}, \quad \beta_{\rm H} = \beta_r + \beta_m, \quad \alpha_{\rm B} = -\frac{5x_3 + 8x_4}{2(5-x_4)},\\
\gamma_{\rm H} &= \sqrt{(c_r^2 - c_{\rm H}^2 + \beta_{\rm H})^2 + 2c_r^2\alpha_{\rm H}\beta_r}\,.
\end{aligned} \tag{4.42}$$

When $|\alpha_{\rm H}| \ll 1$ we have $c_s^2 \simeq c_{\rm H}^2 - \beta_{\rm H}$ and $\tilde{c}_r^2 \simeq c_r^2 = 1/3$, so the second stability condition (4.41) is satisfied.

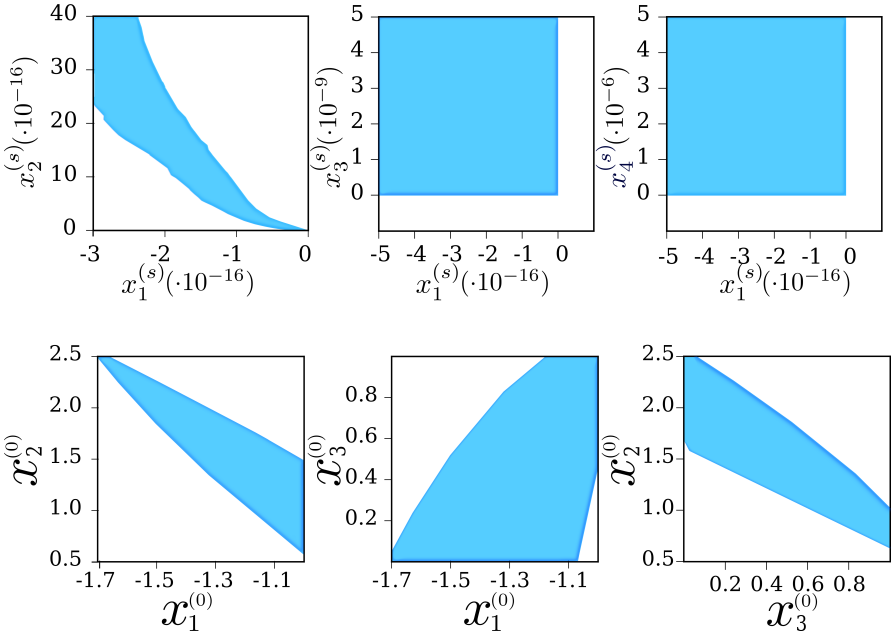

Figure 4.1: The viable parameter space (in blue) for the initial values $x_1^{(s)}$, $x_2^{(s)}$, $x_3^{(s)}$ and $x_4^{(s)}$ at the redshift $z_s = 1.5 \times 10^5$ (top panel) and today's parameters $x_1^{(0)}$, $x_2^{(0)}$ and $x_3^{(0)}$ (bottom panel). In the viable parameter space there are neither ghosts nor Laplacian instabilities.

There are also constraints on today's parameter $\alpha_{\rm H}^{(0)}$ (or equivalently, $x_4^{(0)}$) from massive astrophysical objects [172, 173, 195]. Among those constraints, the orbital period of Hulse-Taylor binary pulsar gives the tightest bound $-0.0031 \leq x_4^{(0)} \leq 0.0094$ [188, 195]. If we literally use the bound arising from the absence of the GW decay into dark energy at LIGO/Virgo frequencies, the parameter $\alpha_{\rm H}^{(0)}$ should be less than the order of 10^{-10} [189]. As we mentioned in Introduction, it is still a matter of debate whether the EFT of dark energy is valid around the frequency $f \sim 100$ Hz [78]. In this work, we will not impose such a bound and independently test how the cosmological observations place the upper limit of $x_4^{(0)}$.

In figure 4.1, we show the physically viable parameter space (blue colored region) for the initial conditions $x_1^{(s)}$, $x_2^{(s)}$, $x_3^{(s)}$, $x_4^{(s)}$ (at redshift $z_s = 1.5 \times 10^5$) and today's values $x_1^{(0)}, x_2^{(0)}, x_3^{(0)}$ (at redshift $z = 0$). We find that $x_1^{(0)}$ is negative, while $x_2^{(0)}$ and $x_3^{(0)}$ are positive. We note that the ghost condensate model [197] has a de Sitter solution satisfying $x_1 < 0$ and $x_2 > 0$. The Galileon term x_3 modifies the cosmological dynamics of ghost condensate, but there is also a de Sitter attractor characterized by $x_1 < 0$, $x_2 > 0$, and $x_3 > 0$ [188]. As we see in figure 4.1, the parameter $x_3^{(0)}$ is not well constrained from the theoretically viable conditions alone.

The parameter space of the variable $x_4^{(0)}$ is not shown in figure 4.1, but it is in the range $|x_4^{(0)}| \ll 1$ to satisfy all the theoretically consistent conditions. As $x_4^{(0)}$ approaches the order 1, the scalar perturbation is typically prone to the Laplacian instability associated with the negative value of c_s^2 [188].

The above results will be used to set theoretical priors for the MCMC analysis.

4.4 COSMOLOGICAL PERTURBATIONS

In this section, we discuss the evolution of scalar cosmological perturbations in the BH model for the perturbed line element given by Eq. (4.9). We introduce the two gauge-invariant gravitational potentials:

$$\Psi \equiv \delta N + \dot{\psi}\,, \qquad \Phi \equiv -\zeta - H\psi\,. \tag{4.43}$$

For the matter sector, we consider scalar perturbations of the matter-energy momentum tensor T^{μ}_{ν} arising from the action $\mathcal{S}_M$, as $\delta T^0_0 = -\delta\rho$, $\delta T^0_i = \partial_i \delta q$, and $\delta T^i_j = \delta P \delta^i_j$. The density perturbation $\delta\rho$, the momentum perturbation δq, and the pressure perturbation δP are expressed in terms of the sum of each matter component, as $\delta\rho = \sum_i \delta\rho_i$, $\delta q = \sum_i \delta q_i$, and $\delta P = \sum_i \delta P_i$, where $i = m, r$. We introduce the gauge-invariant density contrast:

$$\Delta_i \equiv \frac{\delta\rho_i}{\rho_i} - 3H\frac{\delta q_i}{\rho_i}\,, \tag{4.44}$$

where ρ_i is the background density of each component. In the BH model, the full linear perturbation equations of motion were derived in Ref. [188].

In Fourier space with the comoving wavenumber k, we relate the gravitational potentials in Eq. (4.43) with the total matter density contrast $\Delta = \sum_i \Delta_i$, as [119–121]

$$-k^2\Psi = 4\pi G_{\rm N} a^2 \mu(a,k)\rho\Delta\,, \tag{4.45}$$

$$-k^2(\Psi + \Phi) = 8\pi G_{\rm N} a^2 \Sigma(a,k)\rho\Delta\,, \tag{4.46}$$

where $G_{\rm N}$ is the Newton gravitational constant given by Eq. (4.39), and $\rho = \sum_i \rho_i$ is the total background matter density. The dimensionless quantities μ and Σ correspond to the effective gravitational couplings

felt by matter and light, respectively. For nonrelativistic matter, the density contrast Δ_m obeys [188]

$$\ddot{\Delta}_m + 2H\dot{\Delta}_m + \frac{k^2}{a^2}\Psi = -3\left(\ddot{\mathcal{B}} + 2H\dot{\mathcal{B}}\right) , \tag{4.47}$$

where $\mathcal{B} \equiv \zeta + H\delta q_m/\rho_m$. This means that the matter density contrast grows due to the gravitational instability through the modified Poisson Eq. (4.45). In GR, both μ and Σ are equivalent to 1, but in the BH model, they are different from 1. Hence the growth of structures and gravitational potentials is subject to modifications.

For the perturbations deep inside the sound horizon ($c_s^2k^2/a^2 \gg H^2$), the common procedure is to resort to a quasi-static approximation for the estimations of μ and Σ [144, 202, 203]. This amounts to picking up the terms containing k^2/a^2 and Δ_m in the perturbation equations of motion. In Horndeski theories, it is possible to obtain the closed-form expressions for Ψ, Φ, ζ [144, 204]. In GLPV theories, the additional time derivatives $\alpha_{\rm H}\dot{\psi}$ and $\alpha_{\rm H}\dot{\zeta}$ appear even under the quasi-static approximation [169, 205], so the perturbation equations are not closed. If $|\alpha_{\rm H}|$ is very much smaller than 1 and x_4 is subdominant to $x_{1,2,3}$, we may ignore the contributions of the term x_4 to the perturbation equations. In this case, we can estimate μ and Σ in the BH model, as [188]

$$\mu \simeq \Sigma \simeq 1 + \frac{2Q_t x_3^2}{Q_s c_s^2 (2 - x_3)^2} . \tag{4.48}$$

Since μ and Σ are identical to each other, it follows that $\Psi \simeq \Phi$. Under the theoretically consistent conditions (4.36), (4.37), and (4.40), we also have $\mu \simeq \Sigma > 1$ and hence the gravitational interaction is stronger than that in GR. Let us note that in the following we will not rely on this approximation and we will solve the complete linear perturbation equations.

To understand the evolution of perturbations, we consider four different cases (BH1, BH2, BH3, GGC) listed in Table 4.1. The difference

Parameters	BH1	BH2	BH3	GGC
$x_1^{(s)}$ $(\cdot 10^{-16})$	-1	-0.1	-0.01	-1
$x_2^{(s)}$ $(\cdot 10^{-16})$	5	0.05	0.0001	5
$x_3^{(s)}$ $(\cdot 10^{-9})$	1	1	0.1	10
$x_4^{(s)}$ $(\cdot 10^{-6})$	100	1	1	0
$x_1^{(0)}$	-1.37	-1.03	-0.73	-1.23
$x_2^{(0)}$	2.03	1.02	0.12	1.63
$x_3^{(0)}$	0.03	0.69	1.30	0.29
$x_4^{(0)}$	$1 \cdot 10^{-5}$	$5 \cdot 10^{-6}$	$2 \cdot 10^{-4}$	0

Table 4.1: List of starting values of the density parameters x_i at the redshift $z_s = 1.5 \times 10^5$ and corresponding today's values for three beyondHorndeski (BH) models and the Galileon Ghost Condensate (GGC) model with $x_4 = 0$. The BH1, BH2 and BH3 models differ in the starting values $x_i^{(s)}$. All of them satisfy theoretically consistent conditions discussed in Sec. 4.4. We study these models for the purpose of visualizing and quantifying the modifications from ΛCDM. The cosmological parameters (e.g., H_0, Ω_m, Ω_r) used for these models are the Planck 2015 best-fit values for ΛCDM [114].

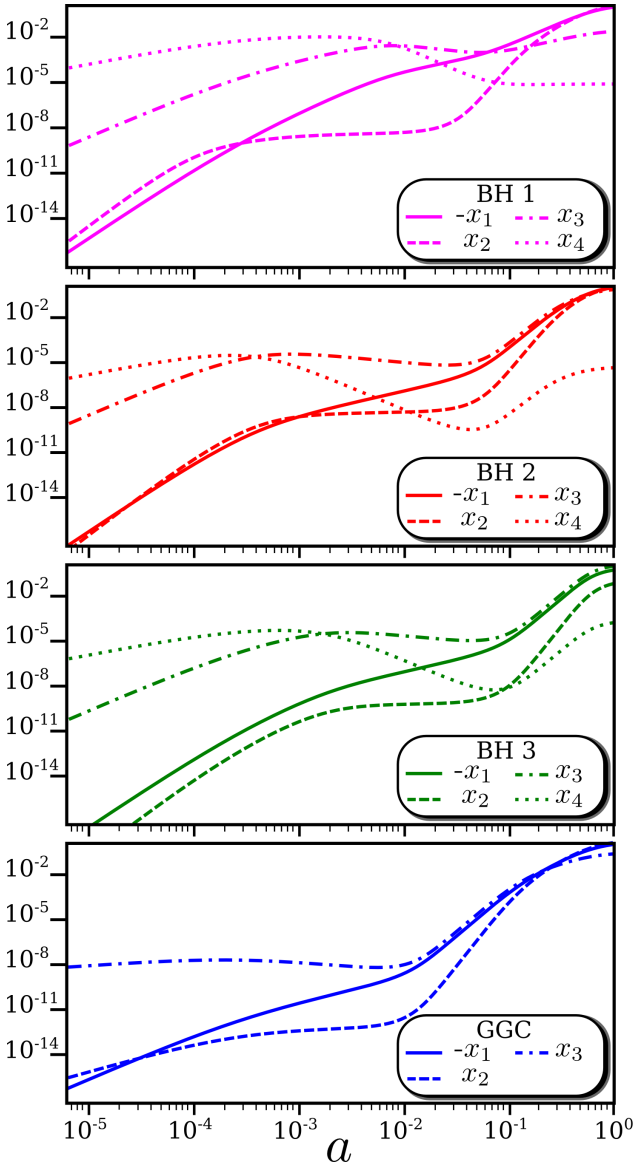

Figure 4.2: Evolution of the dimensionless variables defined in Eq. (4.22) versus the scale factor a (with today's value 1) for four test models listed in Table 4.1. In this Table, the staring values of parameters x_i at the initial redshift $z_s = 1.5 \times 10^5$ are shown for each test model. We discuss physical implications for the evolutions of x_i in Sec. 4.4.

between these models is characterized by the different choices of initial conditions $x_i^{(s)}$ at the redshift $z_s = 1.5 \times 10^5$. Among them, BH1 has the largest initial value $x_4^{(s)}$, while x_4 is always zero in GGC (which belongs to Horndeski theories). In figure 4.2, we plot the evolution of x_i from the past to today for these four different cases. In BH1, the variable x_4 dominates over other variables $x_{1,2,3}$ for $a \lesssim 10^{-2}$, but it becomes subdominant at low redshifts with today's value of order 10^{-5}. Comparing BH1 with BH3, we observe that the initial largeness of x_4 does not necessarily imply the large present-day value $x_4^{(0)}$. At low redshifts, x_4 is typically less than the order 10^{-3} to avoid $c_s^2 < 0$ with the amplitude smaller than $x_{1,2,3}$, in which case the analytic estimation (4.48) can be trustable. Indeed, for all the models given in Table 4.1, we numerically checked that the quasi-static approximation holds with sub-percent precision for the wavenumbers $k > 0.01$ Mpc^{-1} (as confirmed in Horndeski theories in Ref. [81, 201]). In the top panel of figure 4.3, we plot the evolution of Ψ normalized by its initial value $\Psi^{(s)}$ for the four models in Table 4.1 and for the ΛCDM. In the bottom panel, we depict the percentage difference of Ψ for the chosen models with respect to ΛCDM. At the late epoch, the deviations from ΛCDM show up with the enhanced gravitational potential (around $a \sim 0.2$ for the BH2, BH3, GGC models). The largest deviation arises for BH3, in which case the difference is more than 75 % today. As estimated from Eq. (4.48), the modified evolution of Ψ is mostly attributed to the cubic Galileon term x_3. For larger today's values of $x_3^{(0)}$, the difference of Ψ from ΛCDM tends to be more significant with the larger deviation of μ from 1. In figure 4.3, we observe that the deviation from ΛCDM increases with the order of BH1, GGC, BH2, BH3, by reflecting their increasing values of $x_3^{(0)}$ given in Table 4.1.

In BH1, there is the suppression of $|\Psi|$ in comparison to ΛCDM at high redshifts ($a \lesssim 10^{-2}$). This property arises from the dominance of x_4 over $x_{1,2,3}$ at early times, in which case the relative density abundances between dark energy and matter fluids are modified. Besides this effect,

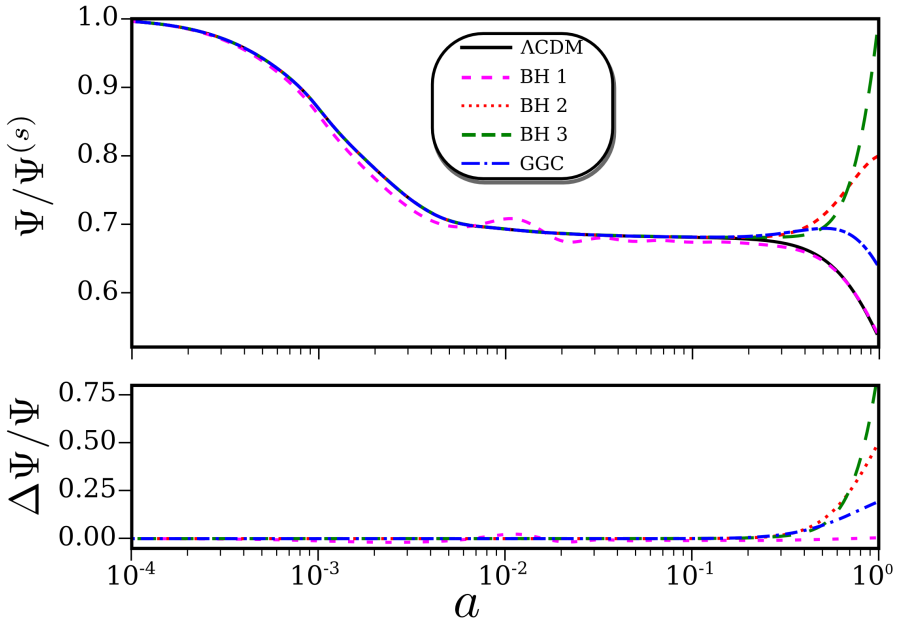

Figure 4.3: (Top) Evolution of the gravitational potential Ψ normalized by its initial value $\Psi^{(s)}$ for the wavenumber $k = 0.01$ Mpc^{-1}. We show the evolution of $\Psi/\Psi^{(s)}$ for four models listed in Table 4.1 and also for ΛCDM (black line). (Bottom) Percentage relative difference of Ψ relative to that in ΛCDM. The cosmological parameters used for this plot are the Planck 2015 best-fit values for ΛCDM [114] (which is also the case for plots in Figs. 4.5 and 4.6). The physical interpretation of this figure is discussed in Sec. 4.4.

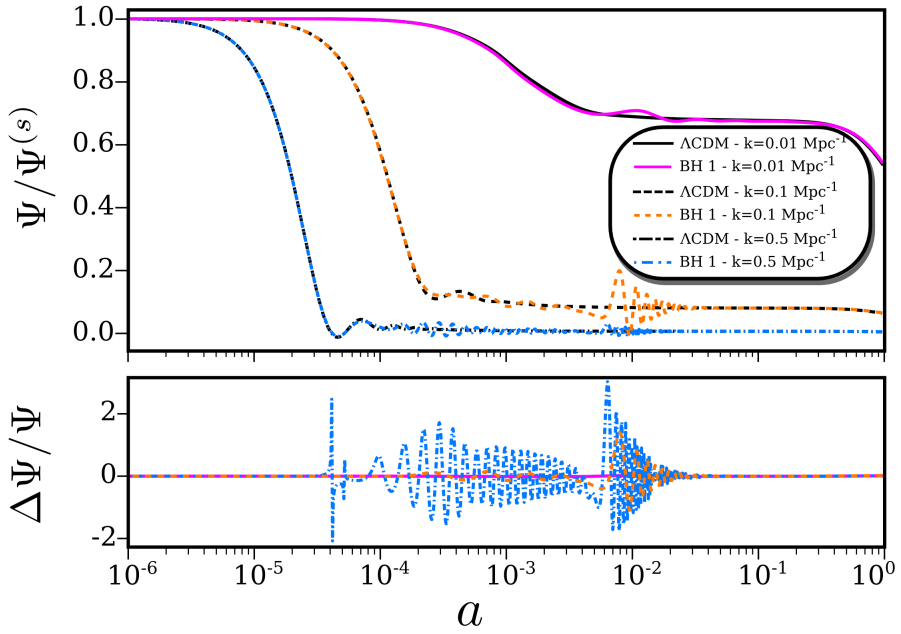

Figure 4.4: (Top) Evolution of the gravitational potential Ψ normalized by its initial value $\Psi^{(s)}$ for BH1 and ΛCDM with three different wavenumbers: $k = 0.01, 0.1, 0.5$ Mpc^{-1}. In Table 4.1, we list the starting values of parameters x_i at the initial redshift $z_s = 1.5 \times 10^5$ for the BH1 model. (Bottom) Percentage relative difference of Ψ relative to that in ΛCDM for the same values of k in the top panel.

the non-negligible early-time contribution of x_4 to scalar perturbations gives rise to a scale-dependent evolution of gravitational potentials, which manifests itself in the k-dependent variation of $\mu(a, k)$ and $\Sigma(a, k)$. In figure 4.4, we plot the evolution of Ψ in BH1 for three different values of k. For perturbations on smaller scales, the deviation from ΛCDM tends to be more significant. In models BH2, BH3, and GGC, the early-time evolution of Ψ is similar to that in ΛCDM, but they exhibit large deviations from ΛCDM at late times.

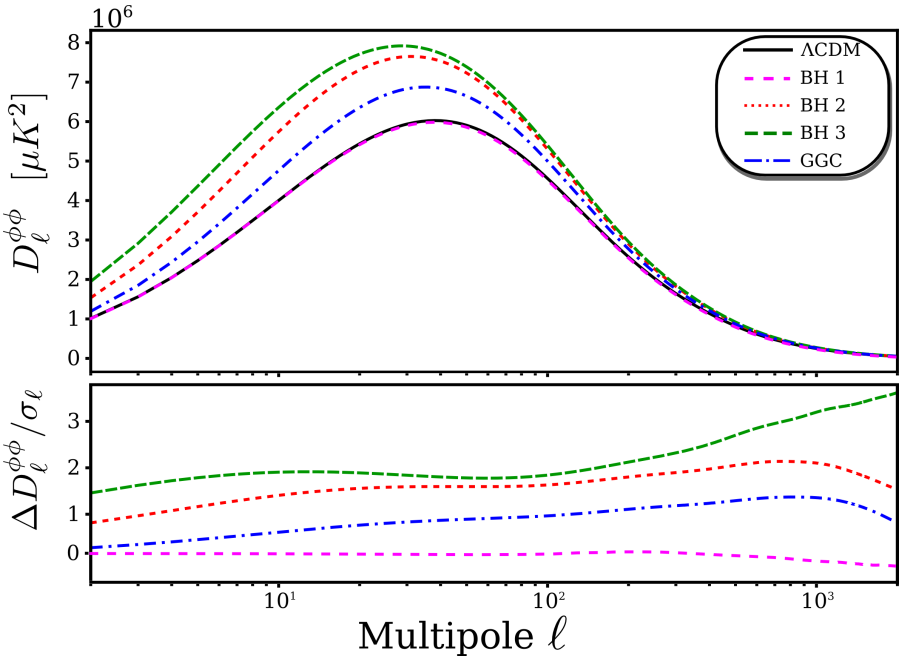

Figure 4.5: (Top) Lensing angular power spectra $D_\ell^{\phi\phi} = \ell(\ell+1)C_\ell^{\phi\phi}/(2\pi)$ for ΛCDM and the models listed in Table 4.1, where C_ℓ is defined by Eq. (4.49). (Bottom) Relative difference of the lensing angular power spectra, computed with respect to ΛCDM, in units of the cosmic variance $\sigma_\ell = \sqrt{2/(2\ell+1)}C_\ell^{\Lambda\,\mathrm{CDM}}$.

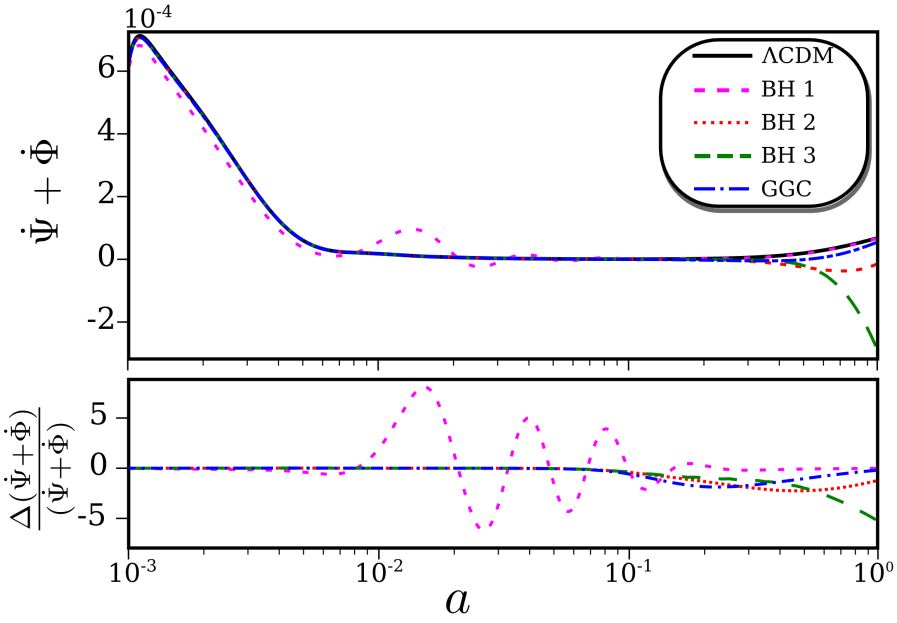

Figure 4.6: (Top) Evolution of the time derivative $\dot{\Psi} + \dot{\Phi}$ for ΛCDM and the models listed in Table 4.1, computed at $k = 0.01$ Mpc^{-1}. (Bottom) Relative difference of $\dot{\Psi} + \dot{\Phi}$, computed with respect to ΛCDM. See the discussion after Eq. (4.53) for the physical interpretation of this figure.

At low redshifts, the lensing gravitational potential $\phi_{\rm len} = (\Psi + \Phi)/2$ evolves in a similar way to Ψ, by reflecting the property $\mu \simeq \Sigma$ for $x_4^{(0)} \ll 1$. The lensing angular power spectrum can be computed by using the line of sight integration method, with the convention [206]

$$C_\ell^{\phi\phi} = 4\pi \int \frac{{\rm d}k}{k} \mathcal{P}(k) \left[\int_0^{\chi_*} {\rm d}\chi \, S_\phi(k; \tau_0 - \chi) j_\ell(k\chi) \right]^2 , \tag{4.49}$$

where $\mathcal{P}(k) = \Delta^2_{\mathcal{R}}(k)$ is the primordial power spectrum of curvature perturbations, and j_ℓ is the spherical Bessel function. The source S_ϕ is expressed in terms of the transfer function

$$S_\phi(k; \tau_0 - \chi) = 2T_\phi(k; \tau_0 - \chi) \left(\frac{\chi_* - \chi}{\chi_* \chi} \right) , \tag{4.50}$$

with $T_\phi(k, \tau) = k\phi_{\rm len}$, χ is the comoving distance with χ_* corresponding to that to the last scattering surface, τ_0 is today's conformal time $\tau = \int a^{-1} \, {\rm d}t$ satisfying the relation $\chi = \tau_0 - \tau$. In figure 4.5, we show the lensing power spectra $D_\ell^{\phi\phi} = \ell(\ell+1) C_\ell^{\phi\phi}/(2\pi)$ and relative differences in units of the cosmic variance for four models listed in Table 4.1. Since $\Sigma > 1$ at low redshifts in BH and GGC models, this works to enhance $D_\ell^{\phi\phi}$ compared to ΛCDM. We note that the amplitude of matter density contrast δ_m in these models also gets larger than that in ΛCDM by reflecting the fact that $\mu > 1$. In figure 4.5, we observe that, apart from BH1 in which Σ is close to 1, the lensing power spectra in other three cases are subject to the enhancement with respect to ΛCDM. Since today's values of μ and Σ increase for larger $x_3^{(0)}$, the deviation from ΛCDM tends to be more significant with the order of GGC, BH2, and BH3.

Let us proceed to the discussion of the impact of BH and GGC models on the CMB temperature anisotropies. The CMB temperature-temperature (TT) angular spectrum can be expressed as [207]

$$C_\ell^{\rm TT} = (4\pi)^2 \int \frac{{\rm d}k}{k} \, \mathcal{P}(k) \left| \Delta_\ell^{\rm T}(k) \right|^2 , \tag{4.51}$$

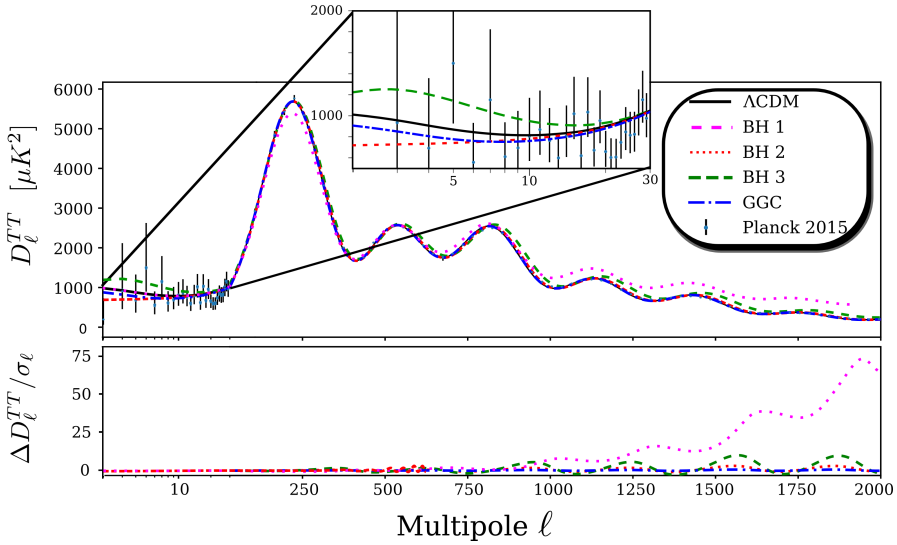

Figure 4.7: (Top) CMB TT power spectra $D_\ell^{\mathrm{TT}} = \ell(\ell+1)C_\ell^{\mathrm{TT}}/(2\pi)$ for the test models presented in Table 4.1, compared with data points from the Planck 2015 release. (Bottom) Relative difference of TT power spectra, computed with respect to ΛCDM in units of the cosmic variance $\sigma_\ell = \sqrt{2/(2\ell+1)}C_\ell^{\Lambda\ \mathrm{CDM}}$.

where

$$\Delta_\ell^{\rm T}(k) = \int_0^{\tau_0} {\rm d}\tau\, e^{ik\tilde{\mu}(\tau-\tau_0)} S_{\rm T}(k,\tau) j_\ell[k(\tau_0-\tau)]\,, \tag{4.52}$$

with $\tilde{\mu}$ being the angular separation, and $S_{\rm T}(k,\tau)$ is the radiation transfer function. The contribution to $S_{\rm T}(k,\tau)$ arising from the integrated-Sachs-Wolfe (ISW) effect is of the form

$$S_{\rm T}(k,\tau) \sim \left(\frac{{\rm d}\Psi}{{\rm d}\tau} + \frac{{\rm d}\Phi}{{\rm d}\tau} \right) e^{-\kappa}\,, \tag{4.53}$$

where κ is the optical depth. Besides the early ISW effect which occurs during the transition from the radiation to matter eras by the time variation of $\Psi + \Phi$, the presence of dark energy induces the late-time ISW effect. In the ΛCDM model, the gravitational potential $-(\Psi+\Phi)$, which is positive, decreases by today with at least more than 30 % relative to its initial value (see figure 4.3). As we observe in figure 4.6 we have $\dot{\Psi} + \dot{\Phi} > 0$ in this case, so the ISW effect gives rise to the positive contribution to Eq. (4.51). In figure 4.7, we plot the CMB TT power spectra $D_\ell^{\rm TT} = \ell(\ell+1)C_\ell^{\rm TT}/(2\pi)$ for the models listed in Table 4.1 and ΛCDM. In BH1 the parameter Σ is close to 1 at low redshifts due to the smallness of $x_3^{(0)}$, so the late-time ISW effect works in the similar way to the GR case. Hence the TT power spectrum in BH1 for the multipoles $\ell \lesssim 30$ is similar to that in ΛCDM.

In the GGC model of figure 4.7, we observe that the large-scale ISW tail is suppressed relative to that in ΛCDM. This reflects the fact that the larger deviation of Σ from 1 leads to the time derivative $\dot{\Psi} + \dot{\Phi}$ closer to zero, see figure 4.6. Hence the late-time ISW effect is not significant, which results in the suppression of $D_\ell^{\rm TT}$ with respect to ΛCDM. As the deviation of Σ from 1 increases further, the sign of $\dot{\Psi} + \dot{\Phi}$ changes to be negative (see figure 4.6). The BH2 model can be regarded as such a marginal case in which the large-scale ISW tail is nearly flat. In BH3, the increase of Σ at low redshifts is so significant

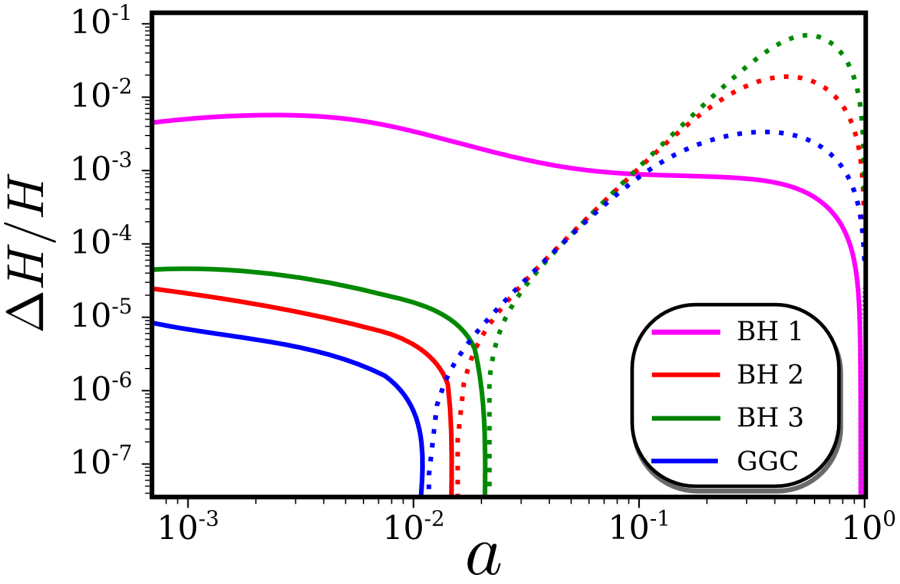

Figure 4.8: Evolution of the relative Hubble rate for the models listed in Table 4.1 compared to ΛCDM. The solid lines correspond to a positive difference, whereas the opposite holds for the dashed lines. For BH1 the largest difference from ΛCDM occurs in the early cosmological epoch, in which case the CMB acoustic peaks shift toward lower multipoles.

that the largely negative ISW contribution to Eq. (4.51) leads to the enhanced low-ℓ TT power spectrum relative to ΛCDM.

The modified evolution of the Hubble expansion rate from ΛCDM generally leads to the shift of CMB acoustic peaks at high-ℓ. In figure 4.8, we observe that the largest deviation of $H(a)$ at high redshifts occurs for BH1 by the dominance of x_4 over $x_{1,2,3}$. This leads to the shift of acoustic peaks toward lower multipoles (see figure 4.7). We also find that BH3 is subject to non-negligible shifts of high-ℓ peaks due to the large modification of $H(a)$ at low redshifts, in which case the peaks shift toward higher multipoles. Moreover, there is the large enhancement of ISW tails for BH3, so it should be tightly constrained from the CMB data. We note that the shift of CMB acoustic peaks is further constrained by the datasets of BAO and SN Ia. For BH2 and GGC the changes of peak positions are small in comparion to BH1 and BH3, but still they are in the range testable by the CMB data. Moreover, the large-scale ISW tail is subject to the suppression relative to ΛCDM in BH2 and GGC.

In BH1, we also notice a change in the amplitude of acoustic peaks occurring dominantly at high ℓ. This is known to be present in models with early-time modifications of gravity [208, 209]. The modification of gravitational potentials affects the evolution of radiation perturbations (monopole and dipole) through the radiation driving effect [208, 210], thus resulting in the changes in amplitude and phase of acoustic peaks at high ℓ.

The modified time variations of Ψ and Φ around the recombination epoch also give a contribution to the early ISW effect. This is important on scales around the first acoustic peak, corresponding to the wavenumber $k \simeq 0.016\ \mathrm{Mpc}^{-1}$ for our choice of model parameters. To have a more qualitative feeling of this contribution, we have estimated

the impact of the early ISW effect on $D_\ell^{\rm TT}$ by using the approximate ISW integral presented in Ref. [210]:

$$\int_{\tau_*}^{\tau_0} {\rm d}\tau \left(\frac{{\rm d}\Psi}{{\rm d}\tau} + \frac{{\rm d}\Phi}{{\rm d}\tau} \right) j_\ell \left[k(\tau_0 - \tau) \right] \simeq \left[\Psi + \Phi \right] |_{\tau_*}^{\tau_0} j_\ell(k\tau_0) \,, \quad (4.54)$$

where τ_* is the conformal time at the last scattering. Then, we find a negative difference of about 4.9 % between BH1 and ΛCDM. This is in perfect agreement with the change in amplitude of the first acoustic peak shown in figure 4.7. Thus, the BH models in which x_4 is the dominant contribution to the dark energy dynamics at early times can be severely constrained from the CMB data.

We stress that, in the late Universe, x_4 is typically suppressed compared to $x_{1,2,3}$ for the viable cosmological background, so the main impact on the evolution of perturbations comes from the cubic Galileon term x_3. The analytic estimation (4.48) is sufficiently trustable for studying the evolution of gravitational potentials and matter perturbations at low redshifts. However, we solve the full perturbation equations of motion for the MCMC analysis without resorting to the quasi-static approximation.

4.5 OBSERVATIONAL CONSTRAINTS

We place observational bounds on the BH model by performing the MCMC simulation with different combinations of datasets at high and low redshifts.

4.5.1 *Datasets*

For the MCMC likelihood analysis, based on the `EFTCosmoMC` code, we use the Planck 2015 [91, 114] data of CMB temperature and polarization on large angular scales, for multipoles $\ell < 29$ (low-ℓ TEB likelihood) and the CMB temperature on smaller angular scales (PLIK

TT Likelihood). We also consider the BAO measurements from the 6dF Galaxy Survey [211] and from the SDSS DR7 Main Galaxy Sample [212]. Moreover, we include the combined BAO and RSD datasets from the SDSS DR12 consensus release [213] and the JLA SN Ia sample [214]. We will refer to the full combined datasets as "Full".

Finally, we impose the flat priors on the model parameters: $x_1^{(s)} \in [-10, 10] \times 10^{-16}$, $x_3^{(s)} \in [-10, 10] \times 10^{-9}$, and $x_4^{(s)} \in [0, 10] \times 10^{-6}$. Even by increasing the prior volume by one order of magnitude, we confirmed that the likelihood results are not subject to the priors choice.

4.5.2 *Constrained parameter space of BH*

In this section, we show observational constraints on model parameters in the BH model. We use the datasets presented in Sec. 4.5.1 with two combinations: (i) Planck and (ii) Full. For reference, we also present the results of the ΛCDM model.

In Table 4.2, we show the marginalized values of today's four density parameters $x_i^{(0)}$ with 95 % confidence level (CL) limits. In figure 4.9, we plot the observationally allowed regions derived by two combinations of datasets with the 68% and 95% CL boundaries. The best-fit values of $x_1^{(0)}$ and $x_2^{(0)}$ constrained by the Planck data are not affected much by including the datasets of BAO, SN Ia, and RSDs. In the observationally allowed region we have $x_1^{(0)} < 0$ and $x_2^{(0)} > 0$, but there are neither ghosts nor Laplacian instabilities in the constrained parameter space (as in the ghost condensate model [197]).

With the Planck data alone, the 95 % CL upper bound on $x_3^{(0)}$ is close to 1, but the Full datasets give the tighter limit $x_3^{(0)} \leq 0.27$ at 95 % CL. The maximum likelihood value of $x_3^{(0)}$ derived with the Planck data is 0.34, which is similar to the corresponding value 0.27 constrained with the Full dataset. The non-vanishing best-fit value of $x_3^{(0)}$ is attributed to the facts that, relative to ΛCDM, (i) the Galileon term can suppress the

Parameters	Planck	Full
$x_1^{(0)}$	$-1.32^{+0.21}_{-0.12}$ (-1.25)	$-1.35^{+0.01}_{-0.06}$ (-1.25)
$x_2^{(0)}$	$1.85^{+0.33}_{-0.69}$ (1.62)	$1.98^{+0.14}_{-0.29}$ (1.68)
$x_3^{(0)}$	$0.16^{+0.54}_{-0.18}$ (0.34)	$0.07^{+0.2}_{-0.1}$ (0.27)
$x_4^{(0)}(\cdot 10^{-6})$	$0.7^{+2.2}_{-1.8}$ (0.15)	$0.3^{+0.7}_{-0.6}$ (0.54)

Table 4.2: Marginalized values of the model parameters $x_i^{(0)}$ and their 95 % CL bounds, derived by Planck and Full datasets. In parenthesis, we also show the maximum likelihood values of these parameters.

large-scale ISW tale, and (ii) the modified background evolution gives rise to the TT power spectrum showing a better fit to the Planck CMB data at high-ℓ. In figure 4.10, these properties can be seen in the best-fit TT power spectrum of the BH model. Increasing $x_3^{(0)}$ further eventually leads to the enhancement of the ISW tale in comparison to ΛCDM. As we see in BH3 of figure 4.7, the models with large $x_3^{(0)}$ do not fit the TT power spectrum well at high-ℓ either. Such models are disfavored from the CMB data (as in the case of covariant Galileons [32, 33]), so that $x_3^{(0)}$ is bounded from above. The RSD data at low redshifts can be also consistent with the intermediate values of $x_3^{(0)}$ constrained from CMB.

In figure 4.11, we show the evolution of $w_{\rm DE}$ for the best-fit BH model. As discussed in Ref. [188], the existence of x_2 besides x_3 prevents the approach to a tracker solution characterized by $w_{\rm DE} = -2$ during the matter-dominated epoch. The best-fit background solution first enters the region $-2 < w_{\rm DE} < -1$ in the matter era and finally approaches

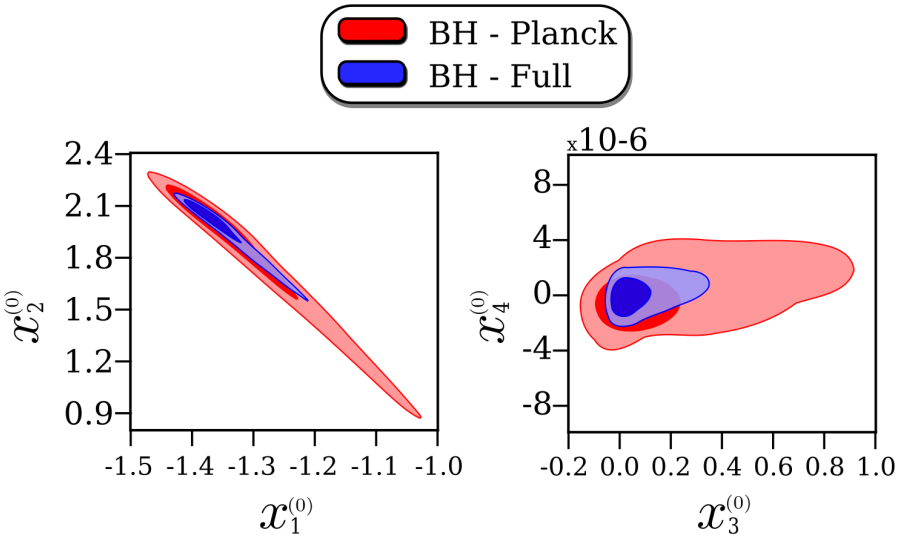

Figure 4.9: Two-dimensional observational bounds on the combinations of today's density parameters $(x_1^{(0)}, x_2^{(0)})$ and $(x_3^{(0)}, x_4^{(0)})$. The colored regions correspond to the parameter space constrained by the Planck (red) and Full (blue) datasets at 68% (inside) and 95% (outside) CL limits.

a de Sitter attractor characterized by $w_{\rm DE} = -1$. Thus, the BH and GGC models with $x_2 \neq 0$ alleviate the observational incompatibility problem of tracker solutions of covariant Galileons [30]. For the best-fit BH model, there is the deviation of $w_{\rm DE}$ from -1 with the value $w_{\rm DE} \approx -1.1$ at the redshift $1 < z < 3$, so the model is different from ΛCDM even at the background level.

From the Full datasets, today's value of x_4 is constrained to be

$$x_4^{(0)} = 0.3^{+0.7}_{-0.6} \times 10^{-6} \quad (95\ \%\ \ \mathrm{CL}), \tag{4.55}$$

so that $|x_4^{(0)}|$ is at most of order 10^{-6}. With the Planck data alone, the upper bound of $|x_4^{(0)}|$ is also of the same order. This means that

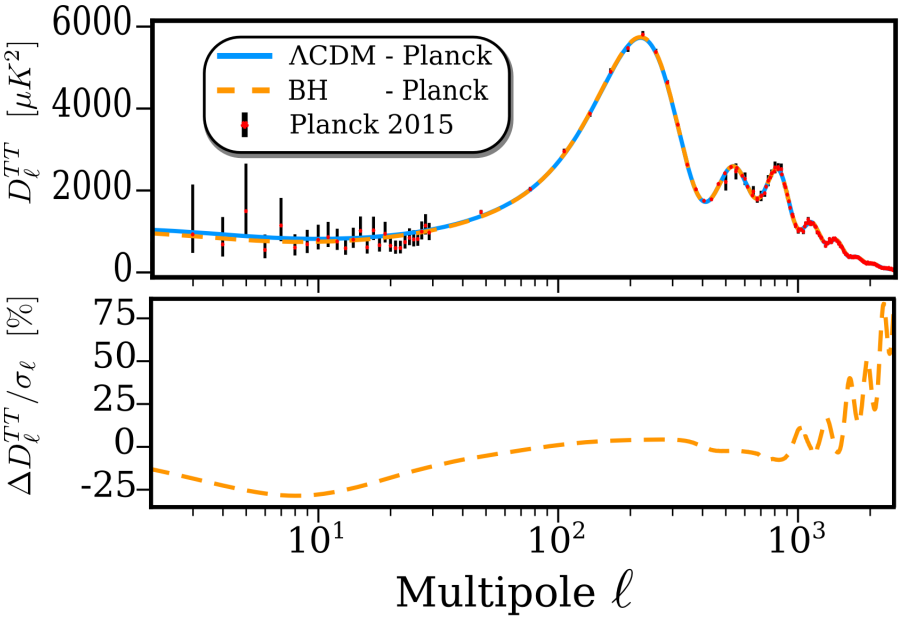

Figure 4.10: (Top) Best-fit CMB TT power spectra $D_\ell^{\mathrm{TT}} = \ell(\ell+1)C_\ell^{\mathrm{TT}}/(2\pi)$ for BH and ΛCDM, obtained with the Planck dataset. The model parameters used for this plot are given in Tables 4.2 and 4.3. For comparison, we plot the data points from the Planck 2015 release [114]. (Bottom) Relative difference of the best-fit TT power spectra, in units of the cosmic variance $\sigma_\ell = \sqrt{2/(2\ell+1)}C_\ell^{\Lambda\ \mathrm{CDM}}$. See Sec. 4.5.2 for the difference between the best-fit BH and ΛCDM models.

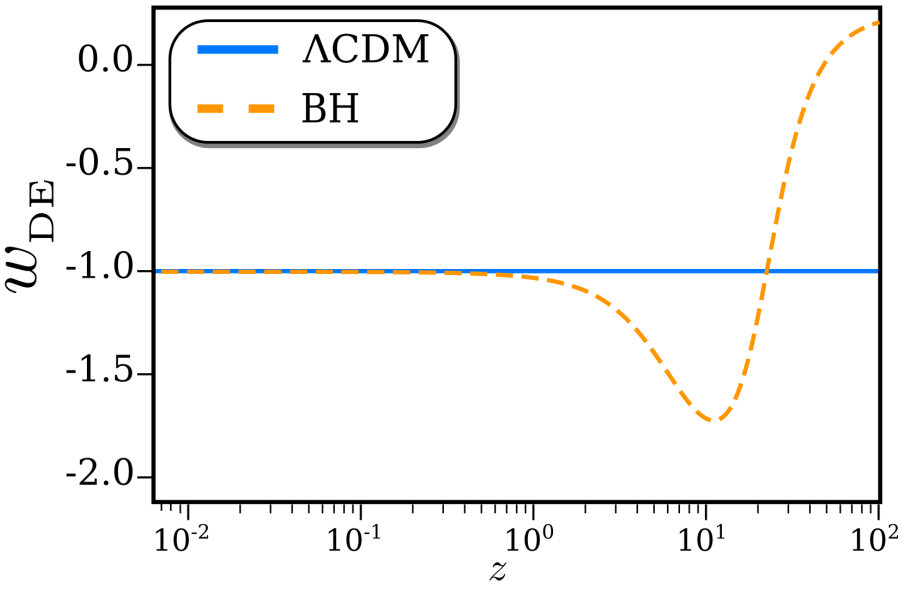

Figure 4.11: Best-fit evolution of the dark energy equation of state $w_{\rm DE}$ for BH and ΛCDM, obtained from the Full analysis. The model parameters used for this plot are given in Tables 4.2 and 4.3. In the best-fit BH, $w_{\rm DE}$ first enters the region $w_{\rm DE} < -1$ and then it finally approaches the asymptotic value $w_{\rm DE} = -1$.

the upper limit of $x_4^{(0)}$ is mostly determined by the CMB data. As we discussed in Sec. 4.4, the CMB TT power spectrum is sensitive to the dominance of x_4 over $x_{1,2,3}$ in the early cosmological epoch. Then, today's value of x_4 is also tightly constrained as Eq. (4.55), which translates to the bound

$$|\alpha_{\rm H}^{(0)}| \leq \mathcal{O}(10^{-6})\,. \tag{4.56}$$

Apart from the constraint arising from the GW decay to dark energy [189], the above upper limit on $\alpha_{\rm H}^{(0)}$ is the most stringent bound derived from cosmological observations so far.

In Table 4.3, we present the values of H_0, $\sigma_8^{(0)}$, and $\Omega_m^{(0)}$ constrained from the Planck and Full datasets for the BH and ΛCDM models. The bounds on H_0, $\sigma_8^{(0)}$, and $\Omega_m^{(0)}$ derived with the Full dataset are similar to those in ΛCDM. In figure 4.12, we also plot the two-dimensional observational contours for these parameters constrained by the Planck data. The direct measurements of H_0 at low redshifts [215] give the

Parameter	Model	Planck	Full
H_0	BH	$68.7^{+3.2}_{-2.8}$ (69.6)	$68.0^{+1.1}_{-1.1}$ (68.2)
	ΛCDM	67.9 ± 2.0 (67.6)	68 ± 1 (68)
$\sigma_8^{(0)}$	BH	$0.849^{+0.037}_{-0.035}$ (0.87)	0.84 ± 0.03 (0.84)
	ΛCDM	0.841 ± 0.03 (0.83)	0.84 ± 0.03 (0.84)
$\Omega_m^{(0)}$	BH	$0.300^{+0.033}_{-0.034}$ (0.28)	$0.306^{+0.014}_{-0.014}$ (0.30)
	ΛCDM	0.30 ± 0.03 (0.31)	0.31 ± 0.01 (0.31)

Table 4.3: Marginalized values of H_0, $\sigma_8^{(0)}$, and $\Omega_m^{(0)}$ and their 95% CL bounds in the BH and ΛCDM models, derived by Planck and Full datasets. The unit of H_0 is km sec^{-1} Mpc^{-1}. In parenthesis, we also show maximum likelihood values of these parameters.

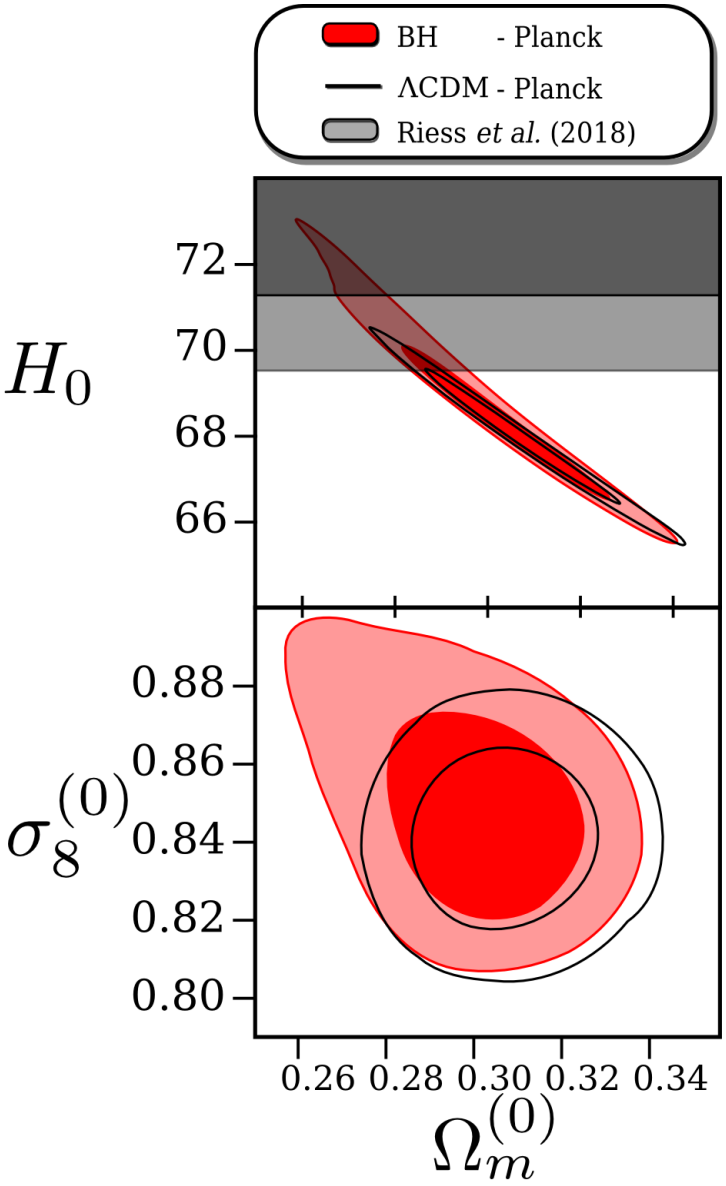

Figure 4.12: The 68 % and 95 % CL two-dimensional bounds on $(H_0, \Omega_m^{(0)})$ (top) and $(\sigma_8^{(0)}, \Omega_m^{(0)})$ (bottom) constrained by the Planck 2015 data, with H_0 in units of $\mathrm{km\,sec^{-1}\,Mpc^{-1}}$. The observational bounds on BH and ΛCDM models are shown as the red and black colors, respectively. In the top panel, the grey bands represent the 68 % and 95 % CL bounds on H_0 derived by its direct measurement at low redshifts [215]. See the last paragraph of Sec. 4.5.2 for the discussion of likelihood results.

bound $H_0 > 70\,\mathrm{km\,sec^{-1}\,Mpc^{-1}}$, whereas the Planck data tend to favor lower values of H_0. Thus, as in the case of ΛCDM, the BH model does not alleviate the tension of H_0 between the Planck data and its local measurements. A similar property also holds for $\sigma_8^{(0)}$, where the Planck data favor higher values of $\sigma_8^{(0)}$ than those constrained in low-redshift measurements. We can also put further bounds on $\sigma_8^{(0)}$ by using the datasets of weak lensing measurements, such as KiDS [86, 112, 216]. For this purpose, we need to take non-linear effects into account in the MCMC analysis, which is beyond the scope of the current chapter.

4.5.3 *Constrained parameter space of GGC*

Since the data are tightly constraining the departures from standard Horndeski gravity (4.56) we decide to perform the same analysis of the previous section also to the Horndeski limit of BH, the GGC model.

In figure 4.13, we plot two-dimensional observational bounds on six parameters by including the Planck+Lensing data as well. Since the beyond Horndeski features were suppressed in BH, we do not see any relevant difference on the cosmological constraints between BH and GGC. Also in this case, the Planck data alone lead to higher values of H_0 than that in ΛCDM, making the former model consistent with the Riess *et al.* bound $H_0 = 73.48 \pm 1.66$ km s^{-1} Mpc^{-1} derived by direct measurements of H_0 using Cepheids [215]. With the Full and CMB lensing datasets, we find that the bounds on H_0, $\sigma_8^{(0)}$ and $\Omega_m^{(0)}$ are compatible between GGC and ΛCDM.

The values of $x_1^{(0)}$ and $x_2^{(0)}$ constrained from the data are of order 1, with $x_1^{(0)} < 0$ and $x_2^{(0)} > 0$. We find the upper limit $x_3^{(0)} < 0.118$ (68 % CL) from the Full data. This bound mostly arises from the fact that the dominance of x_3 over x_2 at low redshifts leads to the enhanced Integrated Sachs-Wolfe (ISW) effect on CMB temperature anisotropies. The most stringent constraints on model parameters are obtained with

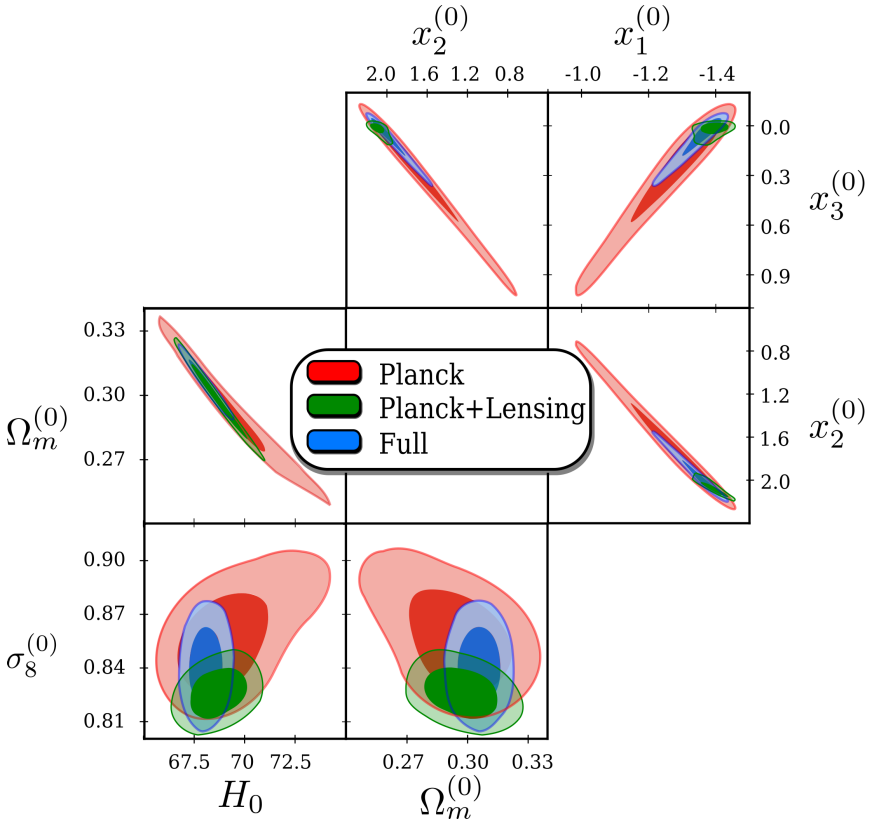

Figure 4.13: Joint marginalised constraints (68 % and 95 % CLs) on six model parameters $x_1^{(0)}, x_2^{(0)}, x_3^{(0)}, H_0, \sigma_8^{(0)}, \Omega_m^{(0)}$ obtained with the Planck, Planck+Lensing, and Full datasets.

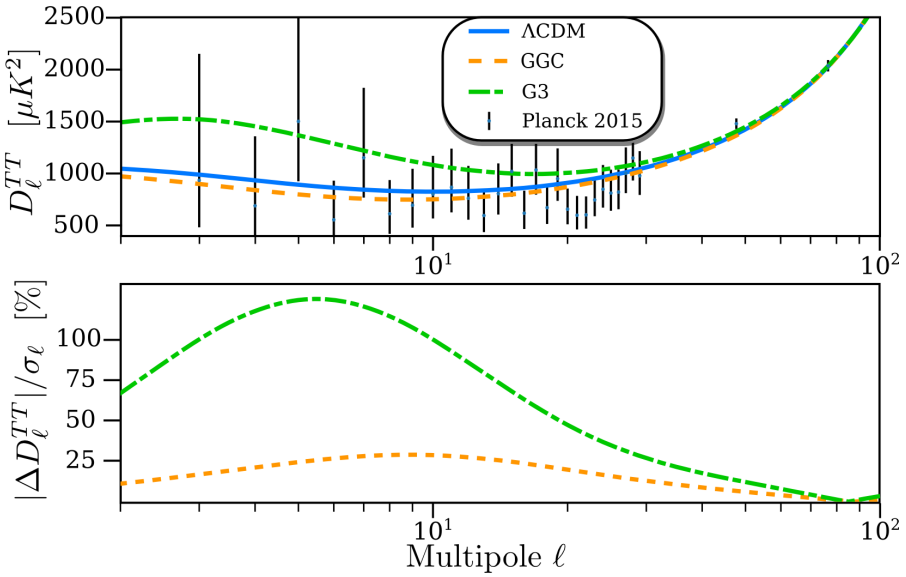

Figure 4.14: *Top panel*: Best-fit CMB temperature-temperature (TT) power spectra $D_\ell^{\mathrm{TT}} = \ell(\ell+1)/2\pi C_\ell^{\mathrm{TT}}$ at low multipoles ℓ for ΛCDM, GGC, and G3 (cubic Galileons), as obtained in the analysis of the Planck dataset. The best-fit values for G3 are taken from Ref. [32]. For comparison, we plot the data points from Planck 2015. *Bottom panel*: Relative difference of the best-fit TT power spectra, in units of cosmic variance $\sigma_\ell = \sqrt{2/(2\ell+1)}C_\ell^{\Lambda\ \mathrm{CDM}}$.

the Planck+Lensing datasets. In figure 4.14, we plot the CMB TT power spectra for GGC as well as for ΛCDM and cubic Galileons (G3), given by the best-fit to the Planck data. The G3 model corresponds to $x_2 = 0$, so that the Galileon density is the main source for cosmic acceleration. In this case, the TT power spectrum for the multipoles $l < \mathcal{O}(10)$ is strongly enhanced relative to ΛCDM and this behavior is disfavored from the Planck data [32].

In GGC, the a_2X^2 term in the action can avoid the dominance of x_3 over x_2 around today. Even if $x_3^{(0)} \ll x_2^{(0)}$, the cubic Galileon gives rise to an interesting contribution to the CMB TT spectrum. As we see

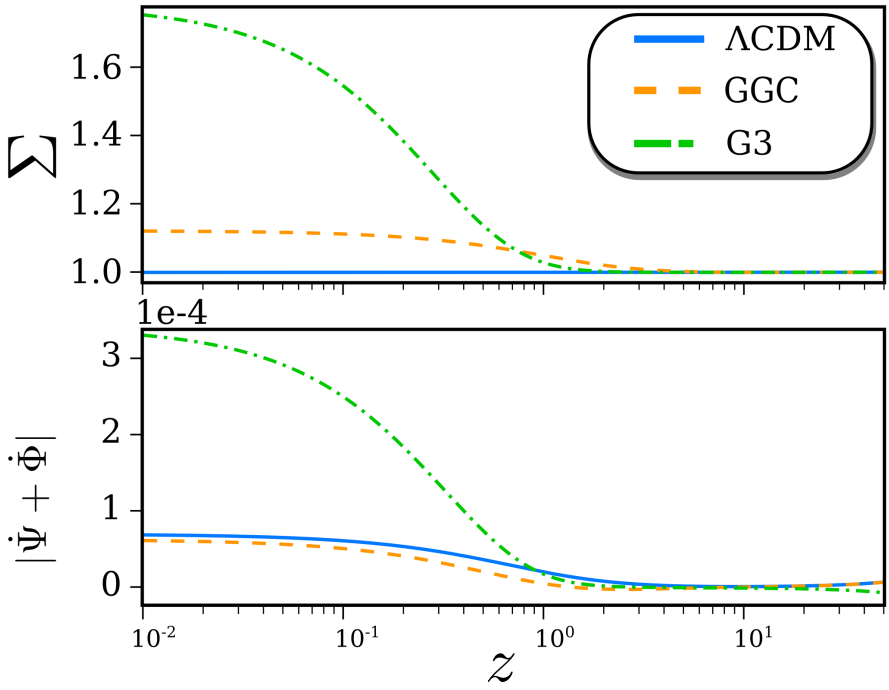

Figure 4.15: Best-fit evolution of Σ (top) and $|\dot{\Psi}+\dot{\Phi}|$ (bottom) versus z at $k = 0.01$ Mpc^{-1} for ΛCDM, GGC, and G3 derived with the Full dataset.

in figure 4.14, the best-fit GGC model is in better agreement with the Planck data relative to ΛCDM by suppressing large-scale ISW tails. Taking the limit $x_3^{(0)} \to 0$, the TT spectrum approaches the one in ΛCDM. The TT spectrum of G3 in figure 4.14 can be recovered by taking the limit $x_3^{(0)} \gg x_2^{(0)}$.

In figure 4.15, we depict the evolution of Σ and $|\dot{\Psi} + \dot{\Phi}|$ for GGC, G3 and ΛCDM, obtained from the Full dataset best-fit. In G3, the large growth of Σ from 1 leads to the enhanced ISW effect on CMB anisotropies determined by the variation of $\Psi + \Phi$ at low redshifts. For the best-fit GGC, the deviation of Σ from 1 is less significant, with $\dot{\Psi} + \dot{\Phi}$ closer to 0. In the latter case, the TT spectrum is suppressed with respect to ΛCDM. This is why the intermediate value of $x_3^{(0)}$ around 0.1 with $x_2^{(0)} = \mathcal{O}(1)$ exhibits the better compatibility with the CMB data relative to ΛCDM.

As we see in figure 4.16, the best-fit GGC corresponds to the evolution of $w_{\rm DE}$ approaching the asymptotic value -1 from the region $-2 < w_{\rm DE} < -1$. This overcomes the problem of G3 in which the $w_{\rm DE} = -2$ behavior during the matter era is inconsistent with the CMB+BAO+SNIa data [30]. This nice feature of $w_{\rm DE}$ in GGC again comes from the combined effect of x_2 and x_3.

4.5.4 *Model Selection*

The BH model has three more parameters compared to those in ΛCDM. This means that the former has more freedom to fit the model better with the data. In order to study whether the former is statistically favored over the latter, we compute the Deviance Information Criterion (DIC) [217]:

$$\mathrm{DIC} = \chi^2_{\rm eff}(\hat{\theta}) + 2p_{\rm D}\,, \tag{4.57}$$

where $\chi^2_{\rm eff}(\hat{\theta}) = -2\ln\mathcal{L}(\hat{\theta})$, and $\hat{\theta}$ is a vector associated with model parameters maximizing the likelihood function $\mathcal{L}$. The quantity $p_{\rm D}$ is

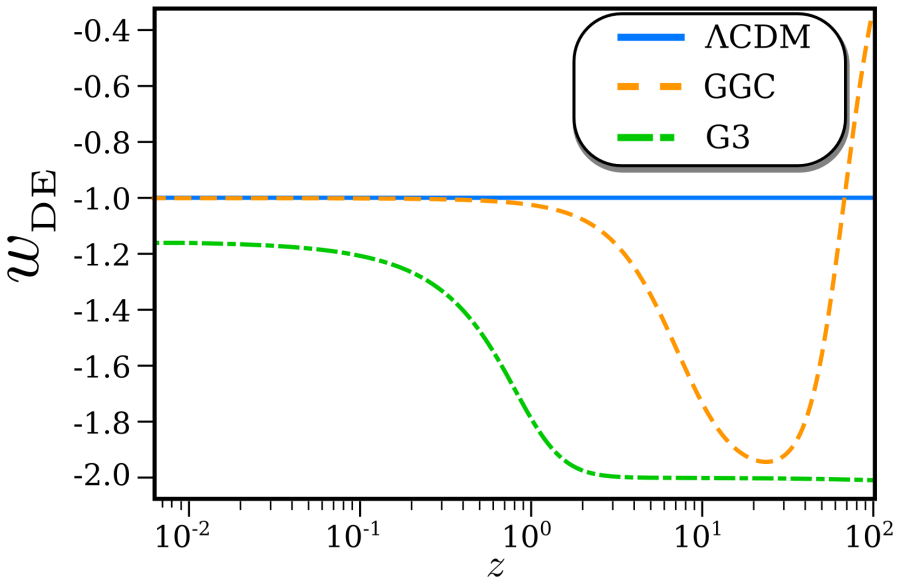

Figure 4.16: Best-fit evolution of $w_{\rm DE}$ versus z for ΛCDM, GGC, and G3 derived with the Full dataset.

Model	Dataset	$\Delta\chi^2_{\rm eff}$	Δ DIC
BH	Planck	-4.7	0.25
BH	Full	-1.8	0.1
GGC	Planck	-4.8	-2.5
GGC	Full	-2.8	-0.6
GGC	Planck+Lensing	-0.9	0.80

Table 4.4: Model comparisons in terms of $\Delta\chi^2_{\rm eff}$ and Δ DIC. As the reference model, we use the value $\chi^2_{\rm eff}$ in ΛCDM. From the definition in (4.58) Δ DIC $>$ 0, indicates that ΛCDM is favored, while Δ DIC < 0 supports the extended model (BH or GGC).

defined by $p_{\rm D} = \bar{\chi}^2_{\rm eff}(\theta) - \chi^2_{\rm eff}(\hat{\theta})$, where the bar represents an average over the posterior distribution. From its definition, the DIC accounts for the goodness of fit, $\chi^2_{\rm eff}(\hat{\theta})$, and the Bayesian complexity of the model, $p_{\rm D}$. The complex models with more free parameters give larger $p_{\rm D}$. To compare the BH model with the ΛCDM model, we calculate

$$\Delta\,\mathrm{DIC} = \mathrm{DIC}_{\rm BH} - \mathrm{DIC}_{\Lambda\,\rm CDM}\,. \tag{4.58}$$

If Δ DIC is negative, then BH is favored over ΛCDM. For positive Δ DIC, the situation is reversed.

In Table 4.4, we present the relative differences of $\Delta\chi^2_{\rm eff}$ and Δ DIC in BH and GGC models, as compared to ΛCDM. Since $\Delta\chi^2_{\rm eff}$ are always negative, these models provide the better fit to the data relative to ΛCDM. In particular, we find that $\Delta\chi^2_{\rm eff}$ constrained by the Planck data alone are smaller than those derived with the Full dataset. This preference of BH over ΛCDM by the Planck data arises from combined effects of the suppressed large-scale ISW tale caused by the Galileon term and the modified high-ℓ TT power spectrum induced by the different background evolution relative to ΛCDM (as shown in figure 4.10). The former contributes by $\sim 20\,\%$ to a better $\chi^2_{\rm eff}$, while the latter to

the remaining $\sim 80\,\%$. We note that a further lowering of the ISW tail is limited by the shift of acoustic peaks at high-ℓ. Such modifications are also subject to further constraints from the datasets of BAO and SN Ia, but the values of $\Delta\chi^2_{\rm eff}$ constrained with the Full dataset are still negative in both BH and GGC models.

According to the DIC, the BH model is slightly disfavored over ΛCDM with the Full dataset. The GGC model, which has one parameter less than those in BH, is favored over ΛCDM with both Planck and Full dataset. In order to investigate this further, we also make use of the Bayesian evidence factor ($\log_{10} B$) along the line of Refs. [218, 219] to quantify the support for GGC over ΛCDM. A positive value of $\Delta \log_{10} B$ indicates a statistical preference for the extended model and a strong preference is defined for $\Delta \log_{10} B > 2$. The values that we get are $\log_{10} B = 4.4$ for Planck, $\log_{10} B = 5.1$ for Full and $\log_{10} B = 1.6$ for Planck+Lensing. For Planck and Full both Δ DIC and $\Delta \log_{10} B$ exhibit significant preferences for GGC over ΛCDM. This suggests that not only the CMB data but also the combination of BAO, SNIa, RSD datasets favors the cosmological dynamics of GGC like the best-fit case shown in Figs. 4.15 and 4.16. With the Planck+Lensing data the $\chi^2_{\rm eff}$ and Bayesian factor exhibit slight preferences for GGC, while the DIC mildly favours ΛCDM (Δ DIC $= 0.8$) . The model selection analysis with the CMB lensing data does not give a definite conclusion for the preference of models. We note that, among the likelihoods used in our analysis, the CMB lensing alone assumes ΛCDM as a fiducial model [220]. This might source a bias towards the latter.

This implies that the existence of an additional parameter x_4 does not contribute to provide better fits to the data. Indeed, today's value of x_4 is severely constrained as Eq. (4.55) mostly from the CMB data. At the same time, this implies that there are no observational signatures for the deviation $\alpha_{\rm H}$ from Horndeski theories. It is interesting to note that the GGC model, which belongs to a sub-class of Horndeski theories, is statistically favored over ΛCDM even with two additional

parameters, but this property does not persist in the BH model due to the extra beyondHorndeski term $\alpha_{\rm H}$ modifying the cosmic expansion and growth histories.

4.6 CONCLUSION

We studied observational constraints on the BH model given by the action (4.1) with the functions (4.7). This model belongs to a subclass of GLPV theories with the tensor propagation speed squared c_t^2 equivalent to 1. The deviation from Horndeski theories is weighed by the dimensionless parameter $\alpha_{\rm H} = 4x_4/(5 - x_4)$, where x_4 is defined in Eq. (4.22). The BH model also has the a_2X^2 and $3a_3X\Box\phi$ terms in the Lagrangian, which allow the possibility for approaching a de Sitter attractor from the region $-2 < w_{\rm DE} < -1$ without reaching a tracker solution ($w_{\rm DE} = -2$).

Compared to the standard ΛCDM model, the beyondHorndeski term x_4 can change the background cosmological dynamics in the early Universe. Since the Hubble expansion rate H is modified by the non-vanishing x_4 term, this leads to the shift of acoustic peaks of CMB temperature anisotropies at high-ℓ, see BH1 in figure 4.7. Moreover, as we observe in figure 4.4, the early-time dominance of x_4 over $x_{1,2,3}$ leads to the modified evolution of gravitational potentials Ψ and Φ in comparison to ΛCDM, whose effect is more significant for small-scale perturbations. This modification also affects the evolution of radiation perturbations and the early-time ISW effect. As a result, the amplitude of CMB acoustic peaks is changed by the x_4 term. These modifications allow us to put bounds on the deviation from Horndeski theories.

The cubic Galileon existing in the BH model leads to the modified growth of matter perturbations and gravitational potentials at low redshifts. Provided that x_4 is subdominant to $x_{1,2,3}$, the dimensional quantities μ and Σ, which characterize the gravitational interactions with matter and light respectively, are given by Eq. (4.48) under the

quasi-static approximation deep inside the sound horizon. Thus, the Galileon term x_3 enhances the linear growth of perturbations without the gravitational slip ($\mu \simeq \Sigma > 1$). This enhancement can be seen in the lensing power spectrum $D_\ell^{\phi\phi}$ plotted in figure 4.5.

For the CMB temperature anisotropies, the late-time modified growth of perturbations caused by the cubic Galileon manifests itself in the large-scale ISW tale. The ISW effect is attributed to the variation of the lensing gravitational potential $\Psi + \Phi$ related to the quantity Σ. Unlike the ΛCDM model in which the time derivative $\dot{\Psi} + \dot{\Phi}$ is positive, the Galileon term x_3 allows the possibility for realizing $\dot{\Psi} + \dot{\Phi}$ closer to zero. In this case, the large-scale TT power spectrum is lower than that in ΛCDM, see GGC and BH2 in figure 4.7. Moreover, the modified background evolution at low redshifts induced by the Galileon leads to the shift of small-scale CMB acoustic peaks toward higher multipoles. If the contribution of x_3 to the total dark energy density is increased further, the ISW tale is subject to the significant enhancement compared to ΛCDM, together with the large shift of high-ℓ CMB acoustic peaks (see BH3 in figure 4.7). These large modifications to the TT power spectrum also arise for covariant Galileons without the x_2 term, whose behavior is disfavored from the CMB data [32, 33]. In the BH model, the existence of x_2 besides x_3 can give rise to the moderately modified TT power spectrum being compatible with the data.

We put observational constraints on free parameters in the BH model by running the MCMC simulation with the datasets of CMB, BAO, SN Ia, and RSDs. With the Planck CMB data, we showed that today's value of x_4 is constrained to be smaller than the order 10^{-6}. Inclusion of other datasets does not modify the order of upper limit of $x_4^{(0)}$, and hence $|\alpha_{\rm H}^{(0)}| \leq \mathcal{O}(10^{-6})$. Apart from the bound arising from the GW decay to dark energy, this is the tightest bound on $|\alpha_{\rm H}^{(0)}|$ derived so far from cosmological observations.

The other dark energy density parameters $x_1^{(0)}, x_2^{(0)}, x_3^{(0)}$ are constrained in a similar way in BH and in GGC. The best-fit value of

$x_3^{(0)}$ is smaller than $|x_1^{(0)}|$ and $x_2^{(0)}$ by one order of magnitude. This intermediate value of $x_3^{(0)}$ leads to the CMB TT power spectrum with modifications at both large and small scales, in such a way that the BH model can be observationally favored over ΛCDM. The evolution of matter perturbations at low redshifts is not subject to the large modification by this intermediate value of $x_3^{(0)}$ in comparison to ΛCDM, so the BH model is also compatible with the RSD data. The best-fit background expansion history corresponds to the case in which $w_{\rm DE}$ finally approaches -1 from the phantom region $-2 < w_{\rm DE} < -1$, whose behavior is consistent with the datasets of SN Ia and BAO. We also showed that, as in the ΛCDM model, the tensions in H_0 and $\sigma_8^{(0)}$ between CMB and low-redshift measurements are not alleviated for the datasets used in our analysis. Future investigations including non-linear effects and additional probes from weak lensing measurements will allow us to shed light on the possibility for alleviating such tensions in the BH model.

To make comparison between BH, GGC and ΛCDM models, we computed the DIC defined by Eq. (4.57) penalizing complex models with more free parameters. In BH, there are three additional parameters than those in ΛCDM. We found that the effective $\chi^2_{\rm eff}$ in BH is smaller than that in ΛCDM for two combinations of datasets (Planck and Full). This is mostly due to both the suppressed ISW tail in BH and the shifts of high-ℓ acoustic peaks of the CMB TT power spectrum. These combined effects allow the BH model to fit the Planck data better. According to the DIC, however, there is a slight preference of ΛCDM over BH with both Planck and Full datasets. The beyondHorndeski term x_4 generally works to prevent better fits to the data. The GGC model, which corresponds to $x_4 = 0$ with one parameter less than those in BH, is statistically favored over ΛCDM both with the DIC and with the Bayes criterion. To the best of our knowledge, there are no other scalar-tensor dark energy models proposed so far showing such novel properties. This surprising result is attributed to the properties

that, for $x_3^{(0)} \ll x_2^{(0)} = \mathcal{O}(1)$, (i) suppressed ISW tails relative to ΛCDM can be generated, and (ii) $w_{\rm DE}$ can be in the region $-2 < w_{\rm DE} < -1$ at low redshifts.

We have thus shown that the deviation from Horndeski theories is severely constrained by the current observational data, especially by CMB. In spite of this restriction, the best-fit BH model gives the DIC statistics smaller than that in ΛCDM. Moreover, the GGC model with $\alpha_{\rm H} = 0$ leads to bayesian preference relative to ΛCDM, even with two additional parameters. Thus, the BH and GGC models are compelling and viable candidates for dark energy.

Further investigations may be performed in several directions. In this work we considered massless neutrinos, but we plan to extend the analysis to include massive neutrinos and inquire about any degeneracy which can arise between such fluid components and modified gravitational interactions. Moreover, it is of interest to investigate cross-correlations between the ISW signal and galaxy distributions, which can be used to place further constraints on BH and GGC models.

4.7 ACKNOWLEDGMENTS

For the work presented in this chapter we thank Matteo Martinelli for support in the numerical implementation. Furthermore we are grateful to N. Bartolo, A. De Felice, R. Kase, M. Liguori, S. Nakamura, M. Raveri and A. Silvestri for useful discussions and comments.